A Comparison of Plunging- and Pitching-induced Deep Dynamic Stall on an SD7003 Airfoil using URANS and LES Simulations

Mario Carta[a], Roberto Putzu[a], Tiziano Ghisu[a,*]

[a]*Department of Mechanical, Chemical and Materials Engineering. University of Cagliari, via Marengo 2, 09123 Cagliari, Italy*

Abstract

Dynamic stall is a fluid dynamics phenomenon experienced by airfoils undergoing a rapid variation in their operating conditions, such as in the presence of pitching or plunging motions, when the effective angle of attack exceeds the static stall angle. The flow field near the airfoil is characterized by the presence of a strong clockwise vortex originating near the leading edge, which is convected downstream along the suction side, generating a low-pressure region and a continuous rise in lift. A controlled form of dynamic stall is involved in the flight mechanism of some natural flapping-wing flyers, and this is currently a matter of interest for the design of biomimetic micro aerial vehicles. Dynamic stall is also responsible for limitations in helicopters' forward-flight velocity, it can lead to flutter in fixed-wing aircraft and vibration-induced damage in wind turbine blades. In this work, 2D URANS and LES numerical simulations have been carried out for incompressible dynamic stall flow cases over an SD7003 airfoil at a Reynolds number of $6 \cdot 10^4$ and at a reduced frequency of 0.25, with the aim of assessing the validity and the role of low fidelity simulations in dynamic stall prediction, at operating conditions relevant for micro air vehicles. Simulations have been conducted both in the case of periodic pitching and plunging, in order to investigate similarities and differences in the resulting flow fields and aerodynamic coefficients. The effect of the reduced frequency on the agreement between 2D URANS and LES has also been evaluated for an airfoil under periodic plunging.

*Corresponding author: t.ghisu@unica.it

Keywords: Dynamic Stall, Airfoils, Plunging, Pitching, URANS, LES

Nomenclature

Acronyms

AoA angle of attack

CFD computational fluid dynamics

CFL Courant Friedrichs Lewy

DTKE dynamic turbulent kinetic energy

LES large eddy simulation

LEV leading edge vortex

LSB laminar separation bubble

QUICK quadratic upstream interpolation for convective kinematics

SIMPLEC semi-implicit method fo pressure-linked equations consistent

SST shear stress transport

TEV trailing edge vortex

URANS unsteady Reynolds-averaged Navier-Stokes

V3 tertiary vortex

Dimensional properties

c airfoil chord [m]

d spanwise extent [m]

D drag force [kg m s^{-2}]

f frequency [s^{-1}]

h vertical position [m]

k kinetic energy [m^2 s^{-2}]

L lift force [kg m s^{-2}]

M moment [kg m^2 s^{-2}]

p pressure [kg m^{-1} s^{-2}]

p_∞ free-stream pressure [kg m^{-1} s^{-2}]

l_0 integral length scale [m]

s curvilinear coordinate [m]

t time [s]

t_c characteristic time [s]

V_∞ free-stream velocity [m s^{-1}]

$\vec{V}$ velocity vector [m s^{-1}]

ϵ dissipation rate [m^2 s^{-3}]

∇ differential operator [m^{-1}]

ω specific dissipation rate [s^{-1}]

Ω vorticity [s^{-1}]

ρ density [kg m^{-3}]

Non-dimensional properties

α_0 angular amplitude

α_e	effective angle of attack
α_m	mean angle of attack
c_d	drag coefficient
c_f	friction coefficient
c_l	lift coefficient
c_m	moment coefficient
c_p	pressure coefficient
h_0	non-dimensional plunging amplitude
k_f	reduced frequency
Re	Reynolds number
y^+	non-dimensional wall distance
Φ	phase angle
π	Archimede's constant
Ω_r	non-dimensional vorticity
ζ	damping coefficient [-]

Subscripts and superscripts

L	LES
U	URANS

1. Introduction

Dynamic stall plays a fundamental role on the aerodynamic characteristics of maneuvering airfoils and wings, or in the presence of sudden variations in the incoming free-stream conditions. One of the technological fields where it was first investigated pertains to the aerodynamics of helicopter blades under high advance ratio operation: the flow over significant portions of the retreating blades can stall, limiting the maximum forward speed of the helicopter [1]. Dynamic stall on helicopter blades may lead to overloading of the trim control systems, strong vibrations and loss of lift [2], or to flutter, due to the airfoil experiencing negative aerodynamic damping during its pitching/plunging motion, with the risk of damaging the blades [3, 4]. This phenomenon has also been investigated in relation to vibration-related stresses occurring in wind turbine blades [5]. Analytical Leishman-Beddoes-based models have been tuned around the typical flow conditions, to accurately predict dynamic stall onset [6] and the consequent torque production deficit [7]. Stall can be caused by rotor misalignment with respect to the wind direction, sudden wind gusts and other phenomena related to upstream flow conditions. Boundary layer transition plays an important role at low Reynolds numbers [8]: an interesting study on the characteristics of the transitional boundary layer for a pitching and plunging airfoil was presented by Akhlaghi *et al.* [9]. Dynamic stall can create the conditions for aeroelastic instability due to negative aerodynamic damping, giving rise to strong vibrations that can cause structural damage in wind turbine blades [10]. The appearence of aerodynamic buffet in the presence periodic airfoil motions has also been the subject of several works [11]. Some of the proposed solutions involve flow control by means of vortex generators [12, 13], plasma actuators [14, 15] with the intent of reducing the force fluctuations created by the stall process. The use of plasma actuators has been extended to turbomachinery blades with the intent of reducing unsteady loads [16]. Other means of active flow control include the use of synthetic pulsating flow injections inside the boundary

layer at the airfoil's suction side [17, 18, 19]. Piezoelectric actuators [20] and morphing leading edge [21, 22] and trailing edge flaps [23] have also been used for flutter suppression. Numerical optimization has been also used to improve the dynamic stall characteristics of a NACA0012 airfoil [24]. Due to the variability of the incoming flow conditions, robust design solutions are recommended [25].

Dynamic stall has also been analyzed in relation to the flight mechanics of natural fliers. Several studies have been carried out on the flapping motion adopted by some species of birds, with the aim of highlighting the relation between airfoil movement parameters and thrust efficiency. Kang *et al.* [26] compared two types of motion for an SD7003 geometry: combined pitch-plunge and simple plunge, respectively resulting in lightly and deeply stalled flows. The propulsion technique adopted by fish and cetaceans [27], as well as birds and insects, with the exception of smaller insects using the Weis-Fogh mechanism [28], is represented by flapping, i.e. combination of periodic pitching and plunging motions suitably out of phase with each other. In several cases of natural flapping, the static stall angle is observed to be abundantly exceeded, which leads to the generation of additional lift from the wing [29]. Geissler and van der Wall [30] demonstrated how a better control of dynamic stall can be achieved by means of dynamic airfoil deformation, leading to higher propulsive efficiency. Sankarasubramanian *et al.* [31] conducted studies on the propulsive efficiency of a plunging airfoil as a function of airfoil thickness-to-chord ratio, motion amplitude and frequency, for conditions representative of natural fliers. A similar study was conducted by Niu *et al.* [32], with the aim of improving the dynamic characterisics of a NACA0012 airfoil. Zhou *et al.* [33] studied the effects of confinment on the dynamic stall of an oscillating NACA0012 airfoil.

The interaction between a flapping airfoil and the flow around it may also result in power extraction from the flow: Kinsey [34] conducted a computational study of airfoils in periodic flapping motion at low Reynolds numbers,

concluding that the amplitude and frequency of the motion have a large effect on the extraction efficiency, which can be as high as 36%. Further increases in efficiency and maximum lift can be achieved with the help of ground effect [35]. An experimental study was carried out by Fenercioglu and Cetiner [36], focusing on the influence of the wake structure on the capability of an airfoil to extract power from the flow, or to generate thrust.

Recent works analyze the effects on dynamic stall of parameters like airfoil thickness [37], wing aspect ratio [38, 39] and flow compressibility [40]. As McCroskey [3] pointed out, the flow field around the airfoil resulting from a periodic plunging motion alone is very similar to the one created in periodic pitching. Studies have been conducted by McGowan *et al.* [41] and Granlund *et al.* [42] on the low Reynolds number pitch-plunge equivalence with a focus on lift coefficient behavior. The authors used Theodorsen's theoretical approach [43] to determine the motion parameters that should be assigned to the pitching and plunging motions in order to achieve lift equivalence from the two movements. When dealing with low amplitudes and frequencies, the theoretically predicted matching is verified by experimental tests and numerical simulations [41]. On the other hand, if amplitude and frequency are increased beyond certain limits, Theodorsen's analytical approach fails, as linear aeroelastic models lose applicability when the effective angle of attack exceeds the critical static stall angle [44]. The loss of predictive capability of the linear model under post-stall conditions is mainly due to the considerable violation of the initial hypothesis of fully attached flow. There are, however, several cases in the literature [45, 26, 46, 47] where Theodorsen's model surprised for its ability to predict the value of the aerodynamic coefficients, even in situations where the initial validity assumptions were evidently violated. The reason for the effectiveness of Theodorsen's model under such conditions is to be found in the dual nature of the lift force, which is partly due to circulation effects, and partly to non-circulatory effects [41]. When the last contribution is predominant, viscous effects (not predicted by linear theory)

lose relevance, allowing to extend the theoretical approach's validity beyond expectation. A numerical analysis highlighting the importance of viscous effects for moving airfoil cases is found in [48].

1.1. Classification

Carr, McAlister and McCroskey [49] performed a series of low-Mach experimental tests with Reynolds Number of $2.5 \cdot 10^6$ on three modified NACA0012 airfoils in periodic (sinusoidal) pitching motion. Their analysis was conducted with the intent of describing the three modes of separation that trigger dynamic stall:

1. abrupt turbulent leading edge separation
2. trailing edge stall
3. leading edge bubble-bursting stall

Dynamic stall is always preceded by a sudden boundary layer separation over the suction side, which occurs during the movement phase where the effective angle of attack is increasing. Depending on the airfoil's geometry, separation can be seen starting from the leading edge region (first mode), trailing edge region (second mode) or it can involve the creation and bursting of a laminar separation bubble (LSB) downstream of the leading edge (third mode). In all cases, the separation will trigger the formation of a clockwise-rotating vortex (in the direction of a positive pitching moment, see Figure 1). This powerful vortex is called the Leading Edge Vortex (LEV) and feeds from the vorticity generated at the airfoil's leading edge [50, 51, 52]. Subsequently, the LEV increases in size and moves toward the trailing edge, creating a powerful suction that causes the lift coefficient to soar and the moment coefficient to stall. At this point, the maximum lift value is reached. At the end of the motion with increasing α, the center of the LEV overhangs the trailing edge, the moment has reached a negative peak and the lift force is rapidly decreasing. When the LEV passes over the trailing edge, the strong depression induced by its presence favors the roll-up of the laminar shear layer emitted from the

pressure side, from which the trailing edge vortex (TEV), also called "shear layer vortex", originates. This second vortex emerges toward the suction side of the airfoil, transitioning to turbulent conditions and gaining space at the expense of the LEV, which in turn is lifted from the wall and stretched in the wake. In addition to LEV and TEV, there is another coherent structure that plays a fundamental role in determining the flow field on the suction side of the airfoil: it consists of an anti-clockwise vortex, called "tertiary vortex", which is formed from the boundary layer of the suction side at half-chord, when the LEV has almost come to overhang the trailing edge. This structure rises behind the LEV and severs the flow string that feeds the former with the vorticity produced at the leading edge [53]. The severed string develops its own clockwise circulation, giving rise to a new swirling region (a second LEV). While this happens, the tertiary vortex loses intensity until it dissolves. When the LEV is finally shed in the wake, it leaves the airfoil in a completely separated flow condition called "full stall", very similar to a static stall. Starting from the leading edge, while the second phase of the movement begins (decreasing α), the boundary layer on the suction side engages in a reattachment process which is finalized only when the airfoil is well below its static stall angle. If the effects of air compressibility become such as to induce the formation of shock waves close to the airfoil, the formation of an LSB can be inhibited by the presence of shock waves [54]. Kim *et al.* [55] carried out a numerical investigation on the effects of compressibility on dynamic stall onset and development, for a pitching VR-12 airfoil in flow conditions representative of a rotorcraft's retreating blade ($Re \approx 10^6$, $Ma = 0.2$–0.4). They found that for a Mach number of 0.4, the dynamic stall onset is dominated by the compressibility effect. Chandrasekhara [56] noted that for Reynolds' numbers smaller than 10^6, on a NACA0012 airfoil, dynamic stall is initiated by the collapse of an LSB even with a Mach of 0.45, while for larger Reynolds' numbers, the dynamic stall is actually shock-induced for Mach greater than 0.45 without any LSB formation. Under such

conditions, the increased presence of elastic phenomena reduces the ability of the boundary layer to tolerate strong adverse-pressure gradients.

The generation mechanism of the LEV which is predominant at low Reynolds numbers sees the formation, evolution and destruction of the so-called laminar separation bubble. Some studies [57, 58] have paid particular attention to this phenomenon: Chandrasekhara and Ahmed [58] describe the LSB as a clockwise-rotating flow region, enclosed by the locally separated boundary layer. During LSB collapse, a gradual increase in local vorticity levels, and, only in the moments that immediately precede the formation of the LEV, a rapid increase in flow speed along the direction normal to the wall, can be seen. The role of the laminar separation bubble (LSB) in LEV formation was clarified in [59], where a pitching airfoil at moderate Reynolds number was simulated numerically. It was found that the process of LEV formation was characterized by the LSB contraction, with high-frequency pressure fluctuations just before LSB-bursting. A three-dimensional computational analysis focusing on the separation modes associated with dynamic stall, in the presence of a side wall, was conducted by Visbal [60] through large eddy simulations on an SD7003 airfoil at $Re = 6 \cdot 10^4$.

The three main motion parameters that determine whether the conditions for dynamic stall are met are mean angle, amplitude and frequency of the motion [61]. Depending on the value of these parameters, different stall regimes can be achieved. A well-known experimental analysis on different dynamic stall regimes was carried out by McCroskey [3] on NACA0012 airfoils, showing the importance of the mean angle. Adopting the definitions given by McCroskey, Marongiu and Tognaccini [57] identified by means of numerical analyses three types of flow conditions on a NACA0012 airfoil in periodic pitching: pre-stall, light stall and deep stall. In the first case (*pre-stall*) the conditions for triggering dynamic stall are not met, as the oscillation does not reach the static stall angle, and the flow does not detach from the airfoil (thus this is not properly a stall case). Depending on the value of the reduced

frequency, there may be a modest symmetric hysteresis of the aerodynamic coefficients, but the phenomenon falls within the type of aeroelastic behavior predicted by Theodorsen's linear model. *Light stall* is created when the moving airfoil reaches the maximum oscillation amplitude by exceeding the static stall angle by a few degrees. In the case of light stall on an oscillating airfoil, there is a hysteresis of aerodynamic coefficients, confined to the angular range where the static stall angle has been exceeded. The hysteresis of the aerodynamic coefficients in *deep stall* conditions is much more pronounced and extended to a large part of the oscillation cycle. It should be noted that the light dynamic stall regime appears to be the one that can most easily lead to flutter [3] due to the significant negative aerodynamic damping. An interesting study on this matter was recently carried out by Mallik and Raveh [62], where the flow features (leading edge suction and TEV) responsible for the negative damping are identified through dynamic modal decomposition. An experimental analysis on flow-induced vibration in the case of deep dynamic stall can be found in [63].

The start and development processes of dynamic stall are greatly influenced by the motion's reduced frequency. The studies carried out in [64, 54] show a direct proportionality between the reduced frequency value and the angle at which the first flow reversal phenomena occur. Albertson [65] showed a direct dependence of stall angle and maximum lift on the reduced pitch rate for a ramping airfoil at $Re = 6 \cdot 10^4$. The dynamic flow phenomena that give rise to coefficient hysteresis are only present if the reduced frequency of airfoil movement exceeds a certain threshold. In this respect, McAlister, Carr and McCroskey [49] propose the classification of the stall type (static vs. dynamic) according to the reduced frequency of the airfoil's motion. They identified quasi-static stall conditions for $k < 4 \cdot 10^{-3}$, while beyond this value one can begin to see the characteristic fluid formations from dynamic stall. The same threshold is indicated by Niven and Galbraith [66]. Leishman [67] argues that up to a reduced frequency value of $5 \cdot 10^{-2}$, dynamic effects are

still negligible. Similar considerations can be found in [68, 69].

1.2. Aims and Structure

The present work has two aims: to further investigate and verify the similarities between the flow fields and aerodynamic coefficients resulting from periodic plunging pitching motions for an SD7003 airfoil, and to assess the validity of two-dimensional URANS (unsteady Reynolds-average Navier-Stokes) simulations against higher-fidelity simulations such as three-dimensional LES (Large Eddy Simulations) for the prediction of dynamic stall. In fact, despite the known limitation of RANS-based solvers in the solution of largely separated flows, 2D URANS approaches continue to be frequently applied in the solution of this type of problems[70, 32, 31, 33, 12, 19, 16, 25, 21, 55, 22, 24, 23, 52, 11]. 3D URANS have not been considered in this work, both because of the significantly larger computational cost, closer to LES than to 2D URANS at the operating conditions under consideration, but also because of the two-dimensional nature of the problem. 3D URANS have been mainly applied to problems presenting variations in the spanwise directions due to geometrical features or non-uniform boundary conditions [38, 18].

Given the computational cost of LES, a particular operating condition (corresponding to a Reynolds number of $6 \cdot 10^4$, a Mach number below the compressibility limit, a reduced frequency of 0.25 and an effective angle of attack ranging from -5.7 to 22.3 degrees) has been selected. These flow conditions were chosen because of the existence of significant literature to be used as a reference and because of the relevance for MAV (Micro Air Vehicles) applications, at this Mach and Reynolds number.

Initially, stationary simulations have been carried out at the two different angles of attack, i.e. 8 and 14 degrees, to verify the ability of the models to simulate pre-stall and post-stall conditions. Then, two dynamic cases (pure pitching and pure plunging) have been considered. The flow structures that develop in larger Reynolds number flows over periodically moving airfoils

and wings are similar to the ones studied in this work (see for example [71]). However, as the cost of a LES scales roughly with the second power of the Reynolds number [72], computational requirements would have been significantly beyond the available resources.

The laws of motion for pitching and plunging are conceived with the intent of having the two cases follow the same evolution for the effective angle of attack. Numerical simulations for all cases include two-dimensional URANS with a four-equation Transition SST $k-\omega$ turbulence model, and three-dimensional LES.

The effect of varying the non-dimensional frequencies has also been studied for the plunging case, to evaluate the applicability of the lower fidelity method at different operating conditions, by comparison with the results from the higher fidelity method.

The paper is structured as follows. Section 2 presents the problems and numerical method used in this work. Sections 3 and 4 focus on the results of numerical simulations under static and dynamic conditions, respectively. Finally, Section 5 summarizes the findings.

2. Numerical Procedure

2.1. Governing Equations

All simulations are carried out with Ansys Fluent 17.0. For the URANS approach with Transition SST k-ω turbulence model, a SIMPLEC scheme is adopted to solve the coupling between the velocity and pressure fields. Viscous terms are discretized with a second order central scheme, while a second order upwind scheme is adopted for convective terms. In LES, the Dynamic Kinetic Energy sub-grid scale model is chosen. Convective terms in the turbulent kinetic transport equation are discretized with a third order QUICK scheme, while all other equations employ the same schemes used for the URANS solver. All simulations are performed in transient mode with an implicit second-order time marching scheme.

A time step of $5 \cdot 10^{-5}$ is used in URANS simulations, corresponding to a maximum CFL of 25, with 20 Gauss-Seidel sub-iterations per time step. For the LES runs, the number of sub-iterations is set to 10, with a time step of $2 \cdot 10^{-6}$, which guarantees a CFL lower than 1 in all the domain. Stationary simulations are run for 60 characteristic times (corresponding to the time required for the flow to travel along the airfoil) as defined in Eq. (3). Calculations for the first 10 characteristic times are used to establish a fully developed flow, and the following 50 times are used to obtain a statistically meaningful average for the flow quantities. Simulations were run on a 6-node dual-Xeon E5-2667 v2 cluster at the University of Cagliari, and required about 8 seconds per time-step, for a total of about 3 weeks for each case.

URANS and LES dynamic (moving airfoil) runs are initialized with the respective converged static (stationary airfoil) counterparts. One simulation period is used to allow the flow to adapt to the airfoil's dynamics, and results are averaged across the following 8 periods. Each period required about a week on the same computing cluster used for static simulations.

Static results will be compared with simulations data from [73], where the implicit LES solver solver was used on a Chimera grid, with a 6-th order compact differencing scheme and a second-order accurate time-stepping algorithm, Dynamic results will be compared with the ones presented in [60], who used the same solver to study the plunging of an SD7003 airfoil at high reduced frequency.

2.2. Simulation Cases and Boundary Conditions

Five cases of flow over an SD7003 airfoil are analyzed, all with inlet Reynolds number of $6 \cdot 10^4$ and inlet Mach number of 0.025. The SD7003 airfoil has a maximum thickness on chord ratio of 8.5% and a maximum chamber on chord of 1.48%. At the simulated flow conditions, the airfoil presents a maximum lift coefficient of 1.02 and a static stall angle of 11° [73]. The flow field is characterized by the presence of an LSB near the leading edge even at moderate angles of attack. For example, at 4° of AoA, flow

separates at 23% chord and reversed flow is present until 55% chord, where transition takes place, followed by reattachment. As the AoA is increased, separation moves upstream and the LSB starts to contract, until at 14° the flow is fully turbulent and separated downstream 55% of chord. For every case, 2D URANS and 3D LES simulations are performed with the intent of comparing the results.

1. static simulations at angles of attack of 8° and 14° (one before and one after stall), with the same flow conditions and geometry used in [73].
2. flow over a plunging airfoil, with the same flow conditions, geometry and plunging motion as in [60]. A schematic of the settings is shown in Figure 1a.

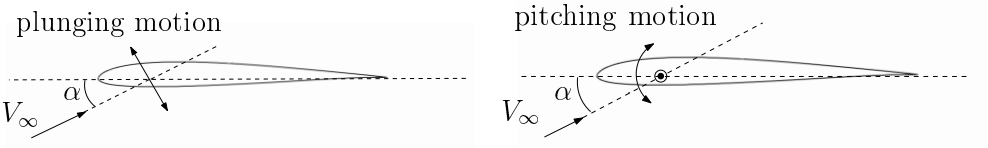

(a) plunging (b) pitching

Figure 1: Schematic of plunging and pitching motions

The plunging motion is described in Eq. (1)

$$h(t) = h_0 c \sin\left(2k_f \frac{t}{t_c}\right) \tag{1}$$

where $h_0 = 0.5$ is the non-dimensional plunging amplitude, $c = 0.1$ m the airfoil chord, k_f the reduced frequency, defined in Eq. (2), and t_c the characteristic time, defined in Eq. (3).

$$k_f = \frac{\pi f c}{V_\infty} = 0.25 \tag{2}$$

$$t_c = \frac{c}{V_\infty} = 0.0114 \text{ s} \tag{3}$$

where V_∞ is the free-stream velocity, and f the frequency of the plunging (or pitching) motion.

The effective angle of attack is described by Eq. (4) [74] and accounts for the relative velocity of the flow field due to the plunging motion. The first term pertains to the fixed geometric angle of attack of $\alpha_m = 8°$.

$$\alpha_e(t) = \alpha_m + \frac{\dot{h}}{V_\infty} \tag{4}$$

3. the third case is the flow over a pitching airfoil. A schematic representing the motion is reported in Figure 1b. The pitching axis is located at the quarter chord.

   The pitching motion is defined to have the same evolution of the effective angle of attack as for the plunging case. This allows a direct comparison between flow structures developed during plunging and pitching. The effective angle of attack for a pitching airfoil is described by Eq. (5), where the oscillation's mean geometric angle of attack is still represented by the fixed value of $\alpha_m = 8°$.

$$\alpha_e(t) = \alpha_m + \alpha_0 \sin\left(2k_f \frac{t}{t_c}\right) + \frac{c\dot{\alpha}}{2V_\infty} \tag{5}$$

   The last term on the right-hand-side of Eq. (5) is the contribution due to dynamic cambering, assumed negligible for reduced frequencies lower than 0.3 [74]. In Figure 2, the effective angle of attack for one period of oscillation is shown, as a function of the phase angle $\Phi = 2k_f t/t_c$. During the upstroke, the static stall angle (11°) is exceeded for a large part of the motion, resulting in a maximum of 22.3°.

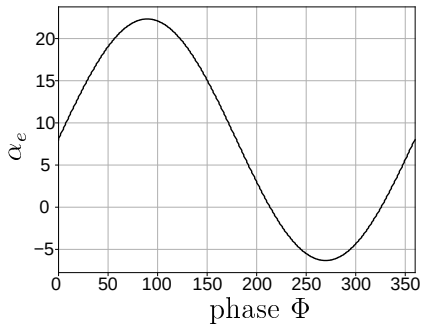

Figure 2: Evolution of the effective angle of attack during one period of oscillation for the plunging and pitching cases.

4. flow over a plunging airfoil, with the same range of angles of attack as in (2) but a larger non-dimensional frequency ($k = 0.5$)
5. flow over a plunging airfoil, with the same range of angles of attack as in (2) but an even larger non-dimensional frequency ($k = 1.0$)

2.3. Grid Structure

Two meshes, one bi-dimensional and one tri-dimensional, are prepared for the purpose of this analysis, the latter having been obtained by extruding the 2D domain in the spanwise direction by a length of $0.1c$. This choice is based on considerations found in [60], and is supported by recent literature ([75] used $s/c = 0.04$, [76] used $s/c = 0.05$, [77] used $s/c = 0.07$, [78] and [79] used $s/c = 0.1$). As additional caution, the effect of a larger spanwise extent ($s/c = 0.2$) has been verified for LES on a static case with an angle of attack of 14 degrees (Section 3.2). The grids are created in Ansys IcemCFD and present a multi-block structured topology, with a circular domain (cylindrical for the 3D version) with the airfoil at the center and a radius of 10 chords. It was found that this distance is enough to consider spurious interaction with the outer boundaries negligible, following a comparison between two domain of 10 and 20 chords radius. Cell sizes throughout the domain are defined according to the turbulence integral length scale criterion: LES simulations require larger turbulent eddies to be resolved by the computational grid, while

the ones smaller than the grid cells are filtered. The grid cell size should therefore be set in order to solve a good fraction of the turbulent kinetic energy k, while the remainder is modeled. Tyacke and Tucker [72] suggest that about 80% of k needs to be solved by the LES approach for the results to be reliable. This requirement is ensured by performing a preliminary 3D steady URANS simulation and evaluating the minimum value of the integral length scale l_0:

$$l_0 = \frac{k^{1.5}}{\epsilon} \tag{6}$$

where ϵ represents the turbulent kinetic energy's dissipation rate. $l_0/5$ is then imposed as limiting value for the maximum cell size, as suggested in [80, 81]. The first cell height (adjacent to the airfoil surfaces) is set to ensure a y^+ value lower than 1, and attention is paid so that the cell aspect ratio is everywhere limited to a maximum value of 5. The amount of turbulent kinetic energy captured by the grid is assessed for the static LES cases with fixed incidence of 8° and 14°. Figure 3 presents the contours of resolved k for LES calculations on the 14° fixed AoA case. More than 90% of k is resolved throughout the whole domain. As an additional verification, a LES simulation for a pitching airfoil has been performed with a smaller mesh, without significant differences in the results (see Section 4.2).

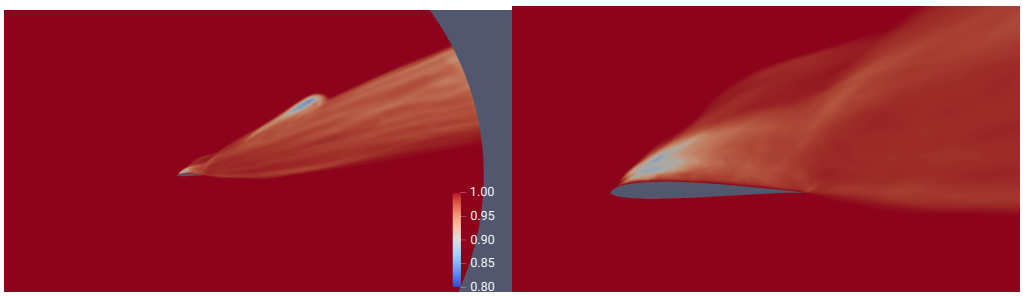

(a) (b)

Figure 3: Fraction of resolved turbulent kinetic energy for LES calculations of static flow at 14 deg of AoA (a) Larger view (b) Airfoil view particular

Figure 4 shows a view of the entire 2D mesh and a close-up around the airfoil. High-refinement regions can be seen near the walls and extending along the wake. The multi-block topology allows for selective refinement, which is implemented by means of a "cut-cell" approach: where needed, cell size is halved going from one block to the adjacent one, keeping a non-conformal (two-in-one) edge between the blocks. The same refinement technique is used in the spanwise direction for the 3D mesh, as shown in Figure 5. Total cell count amounts to 236,304 elements for the 2D grid and 9,497,340 elements for the 3D one. As an additional verification, a URANS simulation for a pitching airfoil has been performed with two smaller meshes, without significant differences in the results (see Section 4.1).

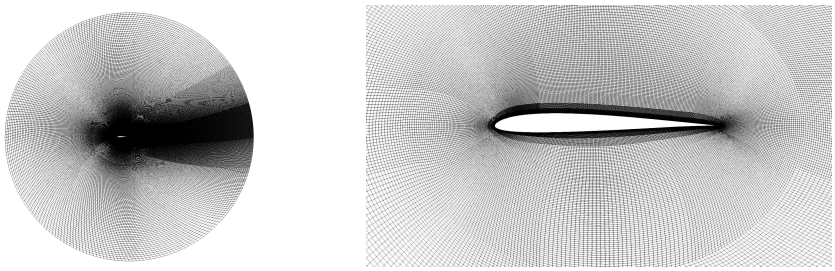

(a) (b)

Figure 4: 2D computational grid used for URANS calculations (a) Entire domain view (b) Airfoil view detail

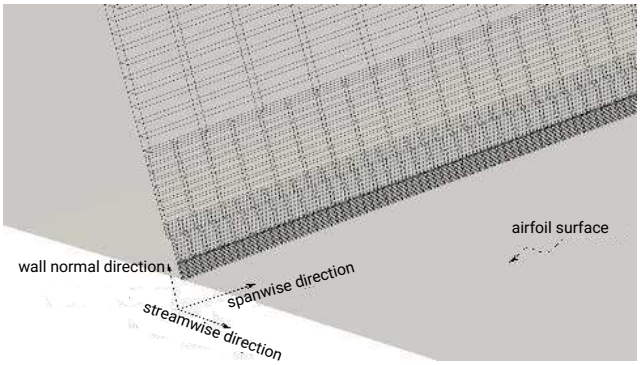

Figure 5: Detail of the 3D mesh structure, for LES simulations

3. Static Simulation Results

3.1. 8 Degrees Angle of Attack

The case with 8° of angle of attack is characterized by the presence of a laminar separation bubble near the leading edge, with boundary layer separation upstream of the bubble, transition to turbulence and downstream reattachment. In Figure 6, the c_p and c_f, defined in Eqs. (7), on the suction side of the airfoil are shown. The presence of an LSB can be discerned from the plateau in the c_p distribution between $s/c = 0.1$ and $s/c = 0.25$ and from the negative peak of the c_f distribution between $s/c = 0.2$ and $s/c = 0.3$, due to the local flow reversal. The subsequent turbulent reattachment is identified by the pressure recovery in the c_p distribution and by the plateau in the c_f distribution, and it is located between $s/c = 0.3$ and $s/c = 0.4$.

$$c_p = \frac{p - p_\infty}{\frac{1}{2}\rho V_\infty^2} \qquad c_f = \frac{\tau_w}{\frac{1}{2}\rho V_\infty^2} \tag{7}$$

where p is the static pressure, ρ the fluid density, and τ_w the wall shear stress, assumed positive when acting in the direction of the drag force. Free-stream conditions are denoted with the symbol ∞.

URANS and LES calculations present the same qualitative curves with the LSB being slightly larger in the LES case. In Figure 7, contours of pressure coefficient are shown: in both solutions, a region of constant c_p on the airfoil's suction side is present, starting from the peak at the leading edge and ending at approximately 1/3 of the chord. In Figure 8, contours of reduced vorticity Ω_r, defined in Eq. (8), are shown. Both models predict a zone of positive vorticity on the airfoil's upper side, from the leading edge up to 1/3 of the chord, which is enclosed by a stream of negative vorticity originating from leading edge. The vorticity shed by the airfoil in the wake is constituted by a negative vorticity contribution from the suction side and positive vorticity from the pressure side.

$$\Omega_r = \frac{\Omega c}{V_\infty} \tag{8}$$

where $\Omega = \nabla \times \vec{V}$ is the vorticity.

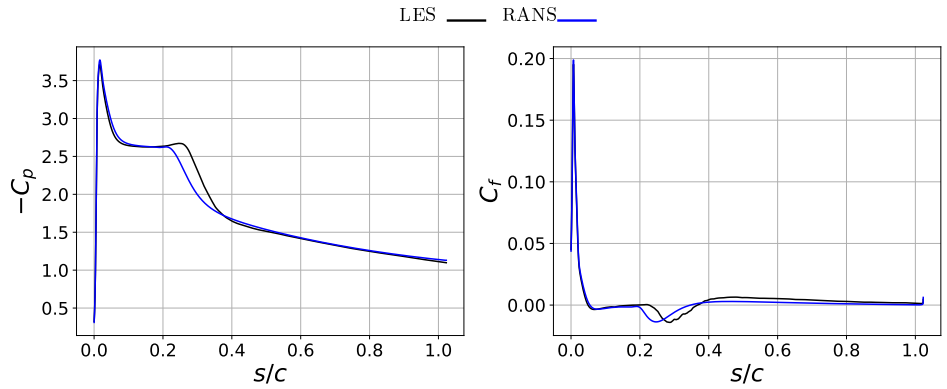

(a) (b)

Figure 6: LES and URANS calculations, 8 deg of AoA. LES values are time-averaged. (a) Pressure coefficient on non-dimensional arc length for airfoil's suction side. (b) Skin friction coefficient on non-dimensional arc length for airfoil's suction side.

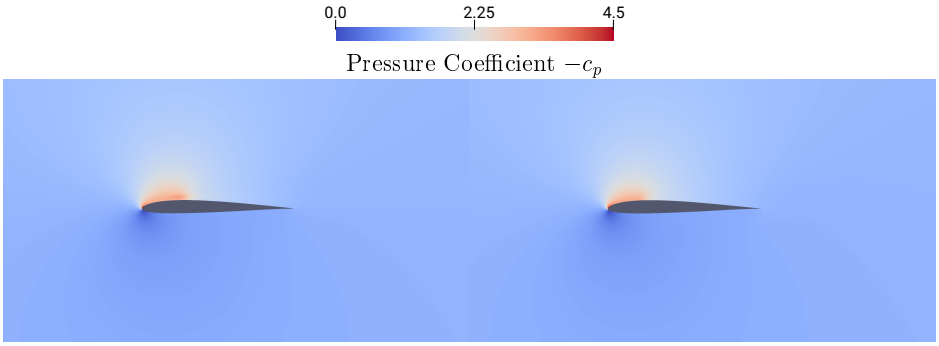

(a) (b)

Figure 7: Pressure coefficient contour plots, 8 deg of AoA. (a) LES calculations, time-averaged flow. (b) URANS calculations.

In Table 1, lift and drag coefficients c_l ad c_d, defined in Eq. (9), are shown, compared with the ones from [73] for the same flow conditions. Experimental measurements performed at the AFRL Water Tunnel and taken from [82] and

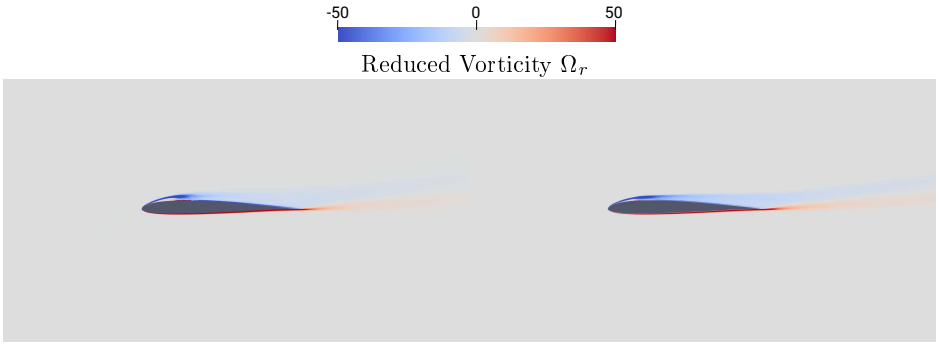

Figure 8: Reduced Vorticity Ω_r contour plots, 8 deg of AoA. (a) LES calculations, time-averaged flow. (b) URANS calculations.

presented in [73] are also reported for comparison. There is good agreement between lift and drag coefficients from LES and URANS calculations of the present work and the ones from [73], with a slight underestimation for the present URANS, especially for the drag coefficient.

$$c_l = \frac{L}{\frac{1}{2}\rho V_\infty^2 cd}; \quad c_d = \frac{D}{\frac{1}{2}\rho V_\infty^2 cd}; \quad c_m = \frac{M}{\frac{1}{2}\rho V_\infty^2 c^2 d} \tag{9}$$

where L and D are lift and drag forces, respectively, and M the moment calculated relative to the airfoil's quarter chord. d is the extension in the perpendicular direction, for 3D simulations.

	c_l	c_d
LES	0.92	0.042
URANS	0.89	0.037
[73]	0.93	0.042
[82]	0.93	-

Table 1: Lift and drag coefficients for LES and URANS calculations for the case at 8 deg of AoA, compared with that from [73] for the same case.

3.2. 14 Degrees Angle of Attack

The case with an angle of attack of 14° is characterized by the presence of a shorter LSB, located more upstream with respect to the previous case. Figure 9 shows the pressure and friction coefficients' behavior. The presence of an LSB can be evinced from the plateau in the c_p distribution at approximately $s/c = 0.1$ and from the negative peak in the c_f distribution around the same position. Due to the airfoil being in post-stall conditions, reversed flow appears downstream of the LSB along with separated boundary layer. However, the presence of a vortex in the time-averaged flow at the airfoil's trailing edge leads to some disagreement between c_p and c_f distribution of LES and URANS calculations. In the LES case, the plateau of c_p extends up to the suction peak at the trailing edge where the vortex core is present.

In Figure 10, pressure coefficient contours are shown: differences between LES and URANS results are evident for the presence of the mentioned suction peak at the airfoil's trailing edge in the LES case. Reduced vorticity contours in Figure 11 show a pair of counter-rotating vortices over the airfoil's trailing edge, responsible for the increased suction. The URANS calculations, on the other hand, only show the positive vorticity from the being shed in the wake. A stream of negative vorticity in both cases starts from leading edge and trails downstream and away from the wall.

In Table 2, lift and drag coefficients are reported, compared with the ones from [73] for the same flow conditions, and to the experimental measurements presented by [82] and used in [73] for comparison. LES have been performed for different spanwise domain extents in order to verify the effect of this parameter. The following simulations have been performed with $s/c = 0.1$ as suggested also in [60]. Several recent works have used smaller or similar spanwise extents ([75] used $s/c = 0.04$, [76] used $s/c = 0.05$, [77] used $s/c = 0.07$, [78] and [79] used $s/c = 0.1$). The present LES results seem to slightly overpredict the lift coefficient with respect to the experimental reference [82], with an error of approximately 5%, while the LES result presented in [73]

is about 9% lower. Given the large variability and uncertainty in post-stall experimental data (see [47]), this result is considered satisfasfactory. The drag coefficient is closer the value obtained by [73], while the experimental result is not available from [47]. URANS simulations underpredict both lift and drag coefficients,. confirming the inability of 2-D URANS calculations to correctly predict post-stall behavior of unforced bluff-body flows, as the associated fluid structures are inherently 3-dimensional.

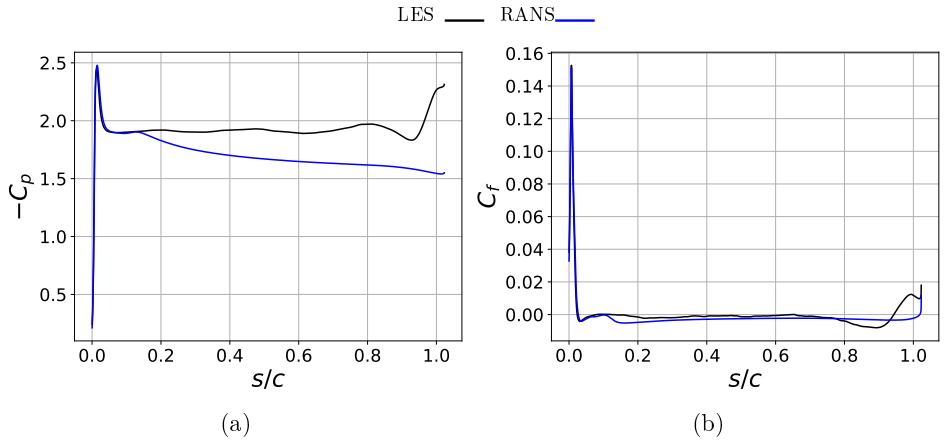

Figure 9: LES and URANS calculations, 14 deg of AoA. LES values are time-averaged. (a) Pressure coefficient on non-dimensional arc length for the airfoil's suction side (b) Skin friction coefficient on non-dimensional arc length for the airfoil's suction side.

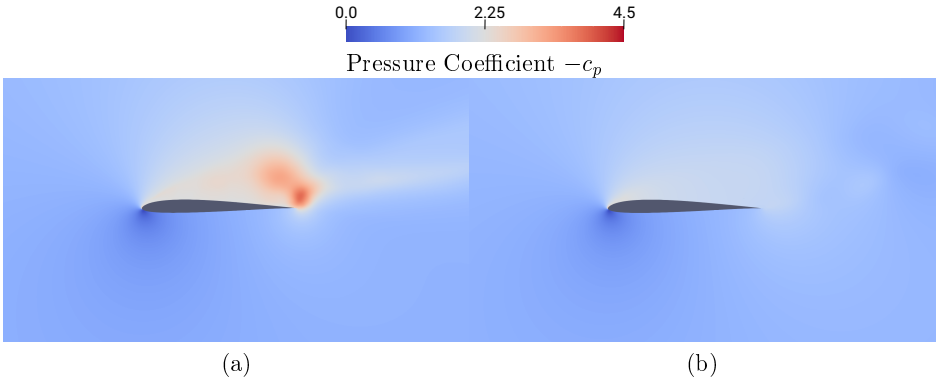

Figure 10: Pressure coefficient contour plots, 14 deg of AoA. (a) LES calculations, time-averaged flow. (b) URANS calculations.

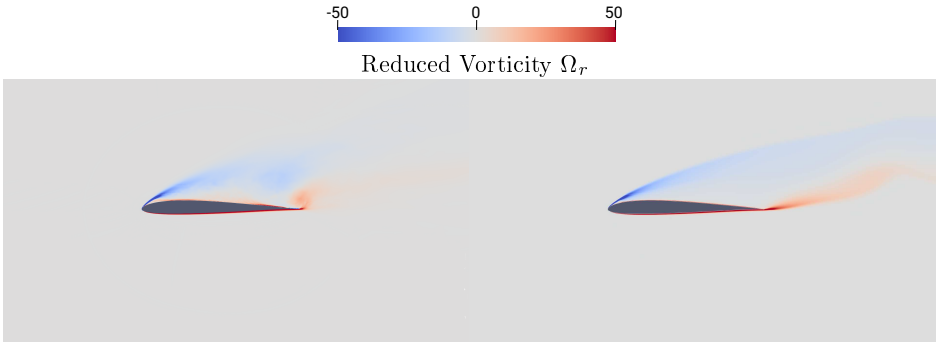

(a) (b)

Figure 11: Reduced Vorticity Ω_r contour plots, 14 deg of AoA. (a) LES calculations, time-averaged flow. (b) URANS calculations.

	c_l	c_d
LES ($s/c = 0.1$)	0.98	0.23
LES ($s/c = 0.2$)	0.99	0.23
URANS	0.75	0.18
[73]	0.89	0.22
[82]	0.94	-

Table 2: Lift and drag coefficients for LES and URANS calculations for the case at 14 deg of AoA, compared with that from [73] for the same case.

4. Dynamics Simulation Results

4.1. 2D URANS Simulations

This section presents a comparison between the 2D URANS flow fields and aerodynamic coefficients resulting from pitching and plunging motions. Simulations are carried out for 9 cycles, and the first one is not used in the phase averaging process. Lift, drag and moment coefficient curves, as a function of the effective angle of attack, are presented in Figures 12(a), 12(b) and 12(c), respectively. The value of the phase angle Φ is indicated next to the curves. Moderate hysteresis of the lift coefficient can be seen, whereas hysteresis of the drag and moment is more pronounced. There is a good agreement between the respective curves for pitching and plunging. In the

lift diagram of Figure 12(a), the hysteresis of the pitching curve is greater than that of the plunging curve, due to the effect of dynamic cambering.

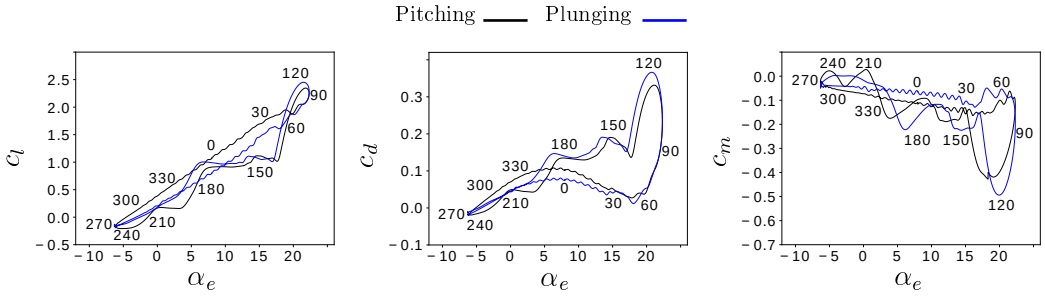

(a) Lift coefficient (b) Drag coefficient (c) Moment coefficient

Figure 12: Phase-averaged lift, drag and moment coefficients as a function of the effective angle of attack, for pitching and plunging motions; URANS calculations.

To ensure that the differences shown in Figure 12 are not affected by an insufficient mesh resolution, considering that the 2D grid used for 2D URANS is constructed with the same density used for LES simulations, a comparison with the results obtained with smaller meshes has been performed. Smaller meshes have been generated by coarsening the finer mesh by a factor of 1.3 in every direction (meshes 1, 2 and 3 had 76,412, 129,728, and 236,304 cells, respectively). Results obtained with grids 2 and 3 were indistinguishable, while the coarsest mesh presented some minor differences at the largest effective angles of attack (Figure 13). The finest mesh was the one used in the article.

To verify the absence of large scale three-dimensional phenomena affecting the flow behavior, a comparison of 2D and 3D URANS (both with $s/c = 0.1$ and $s/c = 0.2$) has been made. Results are presented in Figure 14, and do not present appreciable differences.

In Figures 15 and 16, phase-averaged reduced vorticity contours are presented for the different phases of airfoil movement, along with pressure and skin friction coefficients over the suction side.

Between $\Phi = 0°$ and $\Phi = 30°$, the LSB forms and starts to contract as the effective angle of attack increases. At $\Phi = 30°$, instabilities arise in the

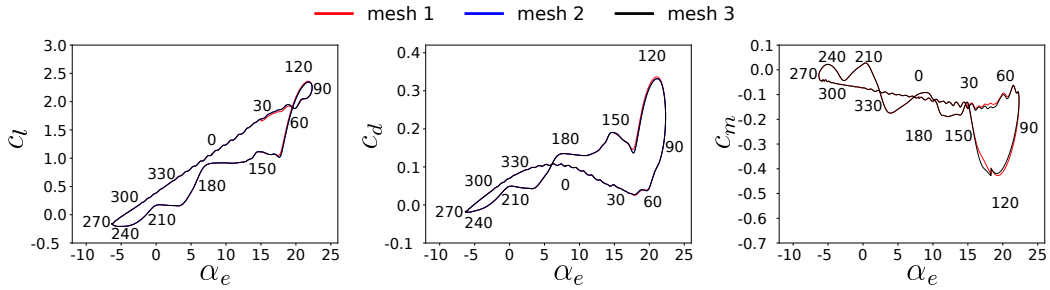

(a) lift coefficient (b) drag coefficient (c) moment coefficient

Figure 13: Comparison of aerodynamic coefficients obtained using 2D URANS and different mesh sizes, for the pitching test case

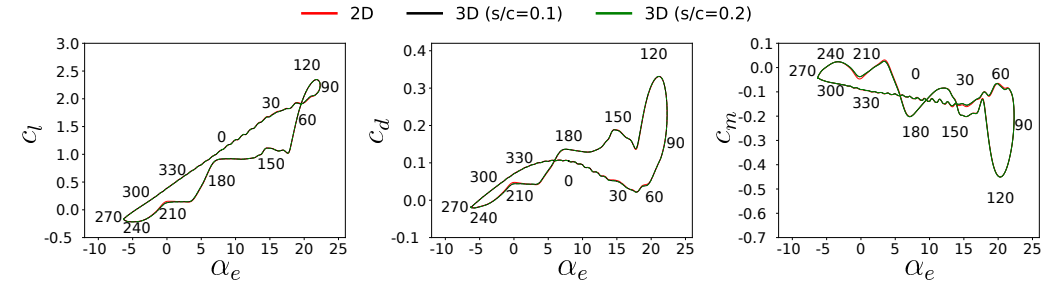

(a) lift coefficient (b) drag coefficient (c) moment coefficient

Figure 14: Comparison of aerodynamic coefficients using 2D and 3D URANS, for the pitching test case

shear-layer along the airfoil's upper side, oscillations appear on c_p and c_f and a pressure peak starts to develop near the leading-edge. The incipient breakdown of the LSB is visible from fluctuations in the plateau of the c_p distribution and in the peak of the c_f distribution, both at approximately s/c = 0.1, corresponding to the position of the LSB. Subsequently, at $\Phi = 60°$, the LEV forms and starts to travel between $s/c = 0.20$ and $s/c = 0.40$. From the reduced vorticity contours at the same phase angle, the LEV can be identified as the negative vorticity region extending from the leading edge to about one third of the chord, while in the c_p contours the same feature can be seen as a low-pressure region. At $\Phi = 90°$, the LEV moves along the airfoil's upper side and the tertiary vortex starts to form, from the roll-up of

the positive vorticity associated with the shear layer enclosed by the LEV.

At $\Phi = 120°$, the tertiary vortex is growing in size and the vortex pair LEV-tertiary is clearly identifiable from the double-peak in the c_p distribution. Between $\Phi = 135°$ and $\Phi = 150°$, the LEV is separated from its feeding sheet by the tertiary vortex. The passage of the LEV over the airfoil's trailing edge induces the formation of a TEV. Between $\Phi = 165°$ and $\Phi = 180°$, LEV, TEV and tertiary vortex are being shed in the wake, while what was previously the feeding sheet of the LEV rolls up over the leading edge to form a last vortex. This secondary LEV then travels downstream and approaches the trailing edge after $\Phi = 180°$. A second tertiary vortex is visible at $\Phi = 165°$, and it separates the secondary LEV into two smaller structures. During the final upstroke, its passage induces a new TEV and in the subsequent phases (after $\Phi = 240°$) the flow returns to a quiescent state, while the c_p and c_f distributions recover to a smoother shape.

Between $\Phi = 0°$ and $\Phi = 90°$, in the c_p distribution, the pitching curve lies above the plunging curve, resulting in the former generating higher lift, as shown in Figure 12(a). Between $\Phi = 120°$ and $\Phi = 270°$, the trend is reversed, resulting in greater lift values generated by the plunging motion. Finally, from $\Phi = 300°$ to $\Phi = 345°$, the pitching curve in the c_p distribution is again above the plunging curve, followed in similar fashion by the lift coefficient. This behavior is caused by the dynamic cambering effects, which start to be noticeable at values of the reduced frequency similar to the one used in this study [74]. Vortical structures during pitching are slightly more pronounced that the analogous ones developed during plunging, with the effect of a larger peak in aerodynamic forces. The same structures appear to be convected faster (Figure 16), with the effect that lift and drag coefficient levels drop faster (Figure 12).

4.2. 3D LES Simulations

This section presents a comparison between 3D LES flow fields and aerodynamic coefficients for the two cases of pitching and plunging. Like for

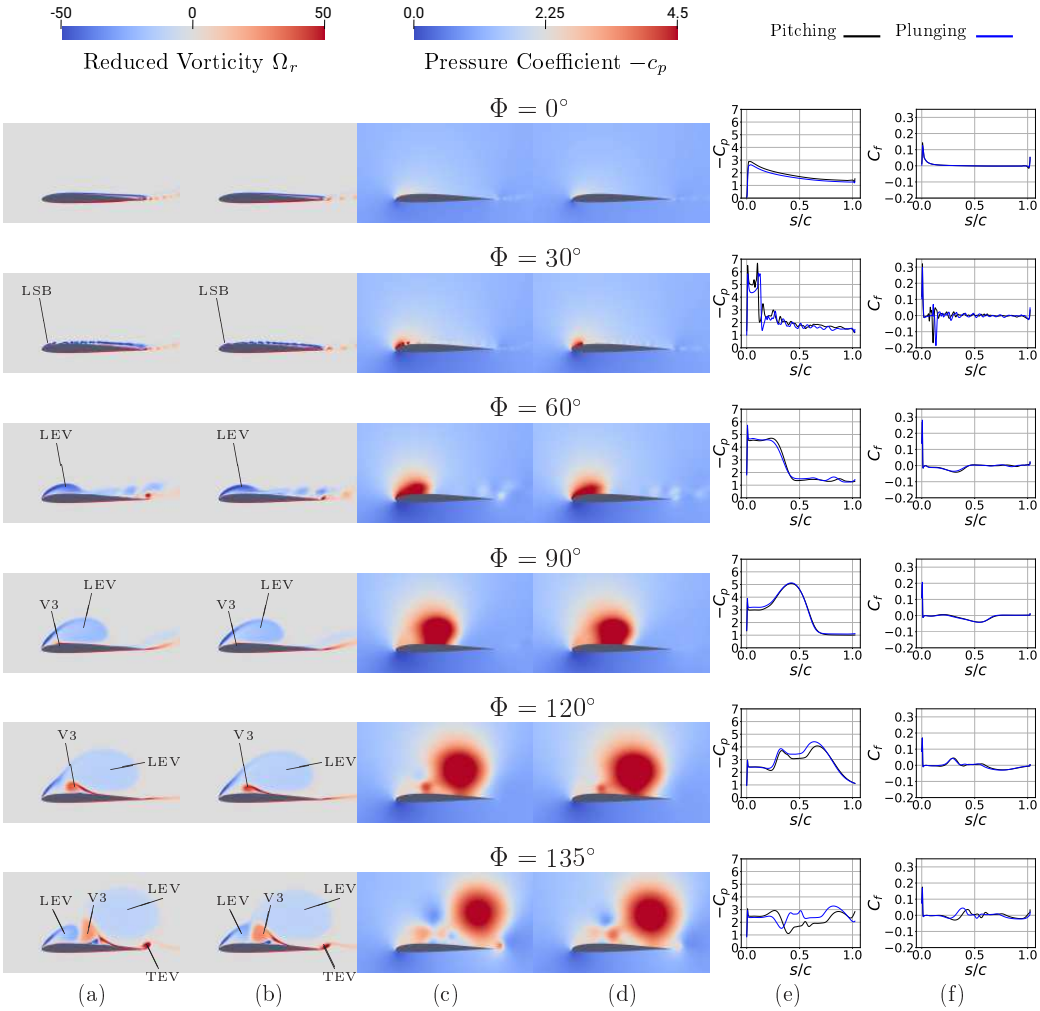

Figure 15: Comparison between phase-averaged pitching and plunging motions for URANS calculations, phase-angle from 0 to 135 degrees. Every row is representative of a phase-angle. Columns (a) and (b) report the contour-plots of reduced vorticity for pitching and plunging motions respectively. Columns (c) and (d) show the contour-plots of the pressure coefficient c_p for pitching and plunging motions respectively. Columns (e) and (f) report, for the airfoil's upper side, pressure and skin-friction coefficient distributions as a function of the non-dimensional axial coordinate.

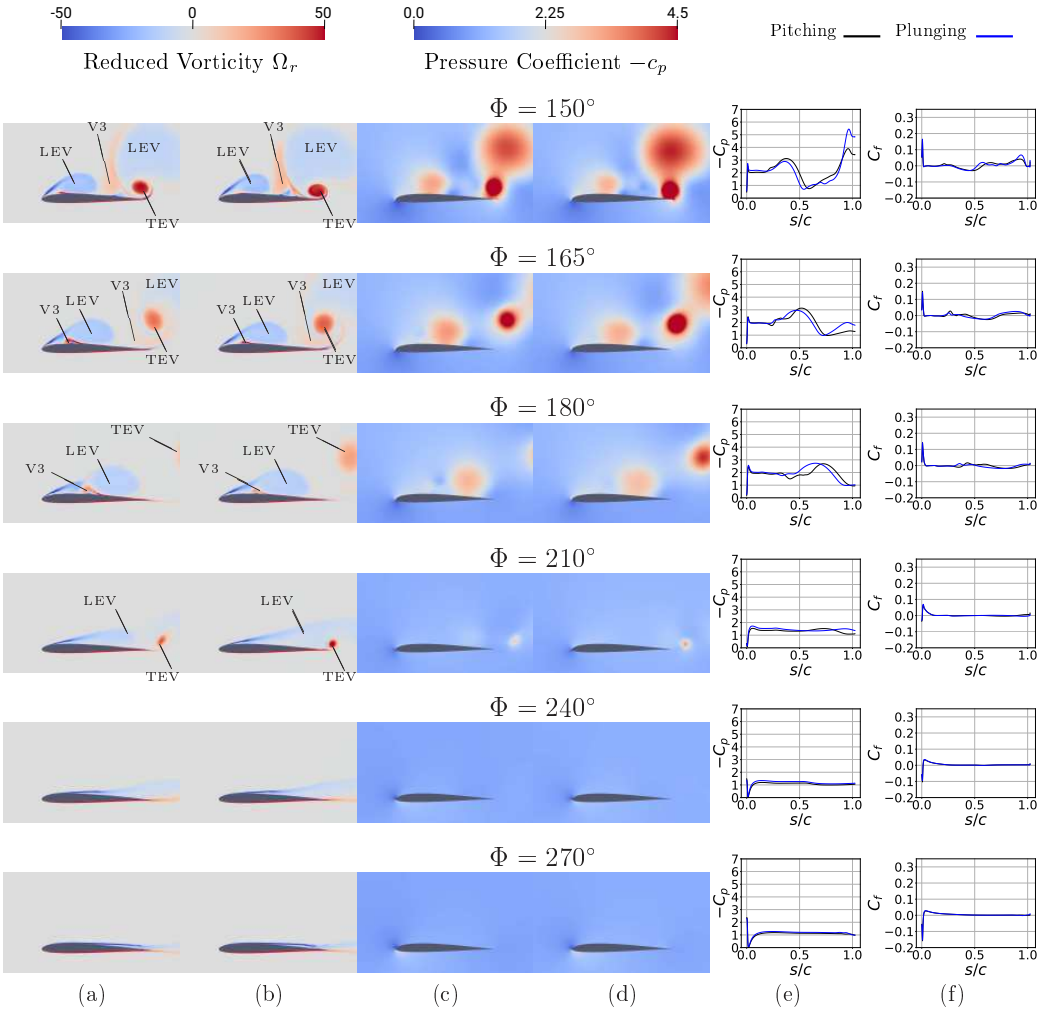

Figure 16: Comparison between phase-averaged pitching and plunging motions for URANS calculations, phase-angle from 150 to 270 degrees. Every row is representative of a phase-angle. Columns (a) and (b) report the contour-plots of reduced vorticity for pitching and plunging motions respectively. Columns (c) and (d) show the contour-plots of the pressure coefficient c_p for pitching and plunging motions respectively. Columns (e) and (f) report, for the airfoil's upper side, pressure and skin-friction coefficient distributions as a function of the non-dimensional axial coordinate.

the previous section, the quantities presented here are the result of a phase-averaging process. Aerodynamic coefficients as functions of the effective angle of attack, are shown in Figures 17(a), 17(b) and 17(c), respectively for lift, drag and moment. As for the analogous plots obtained from URANS simulations (Figure 12), moderate hysteresis can be found in the lift coefficient, whereas hysteresis in the drag and moment curves appears to be more pronounced. There is good agreement between the respective curves for pitching and plunging. It should be noted that, in the lift diagram of Figure 17(a), the hysteresis of the pitching curve is greater than that of the plunging curve. This can be traced down to the effect of dynamic cambering. Visible oscillations are present for Φ ranging approximately from 0 to 30 degrees, due to shear-layer instabilities. For Φ between 30 and 60 degrees, a raise in the moment coefficient is noticeable due to the formation of the LEV. Between $\Phi = 60°$ and $\Phi = 90°$, the moment coefficient drops rapidly as the LEV is convected along the airfoil's upper side, while the drag coefficient continues to rise, mainly due to the presence of flow reversal.

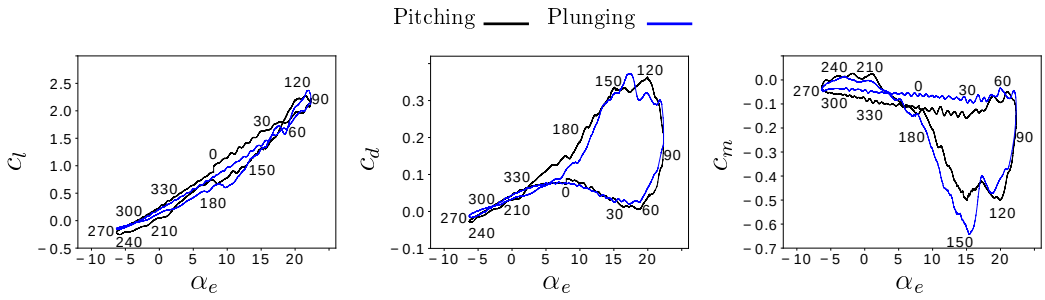

(a) Lift coefficient (b) Drag coefficient (c) Moment coefficient

Figure 17: Phase-averaged lift curve, drag curve and moment curve as a function of the effective angle of attack, for pitching and plunging motions; LES calculations.

To ensure that the differences shown Figure in 17 are not affected by numerical errors, three additional simulations have been run to test the effect of mesh resolution, inlet turbulence intensity, and LES sub-grid scale model. Results are reported in Figure 18, where:

- CASE A has been obtained by uniformly coarsening the reference mesh (reducing the number of edges in every direction by a factor of 1.2). The mesh has a total of 5,467,240 cells, in comparison with 9,497,340 total cells of the reference case

- CASE B has been obtained by increasing the inlet turbulence to 2%, in comparison with the null value of the reference case

- CASE C has been obtained by using the Smagorinsky-Lilly sub-grid scale model, in comparison with the Kinetic-Energy-Transport model used in the reference case

- REFERENCE represents the reference case (used for the analyses presented in this work), with the settings described in Section 2

The comparison is presented in Figure 18 for the pitching case and differences appear to be sufficiently small, considering the intrinsic variability linked to LES simulations, therefore supporting the use of mesh and numerical settings selected.

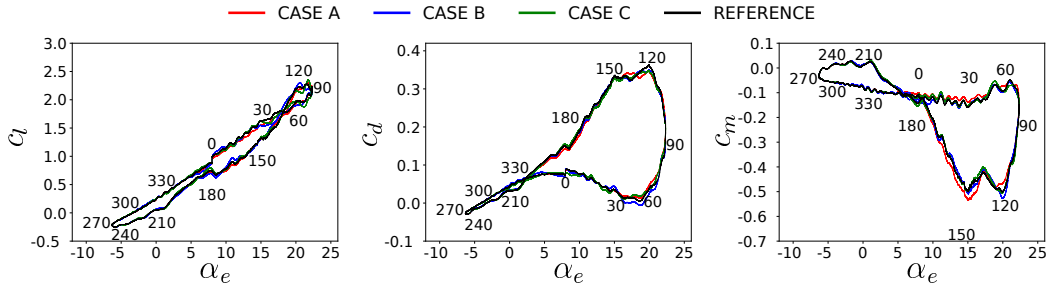

(a) lift coefficient (b) drag coefficient (c) moment coefficient

Figure 18: Comparison of aerodynamic coefficients obtained using LES and different mesh sizes, for the pitching test case

In Figures 19 and 20, phase-averaged reduced vorticity contours are presented for the different phases of airfoil movement, along with pressure and skin friction coefficients over the suction side. Initially, at $\Phi = 0°$, c_p and c_f

distributions are described by smooth curves, with local irregularities due to small-scale vortex shedding and a small separation zone at the trailing edge. The latter is clearly visible from the negative peak in the c_f distribution. When the pitching movement starts its upstroke phase (which corresponds to the downstroke in plunging), precisely between $\Phi = 0°$ and $\Phi = 30°$, a suction peak is visible at the leading edge in the c_p plot, while the LSB forms and starts to contract as the angle of attack increases. At $\Phi = 30°$, the incipient breakdown of the LSB is noticeable from the fluctuations in the c_p and c_f distributions. A single suction peak and a reverse-flow zone are distinguishable, both in the same position as the LSB, for $s/c = 0.1$. At $\Phi = 60°$, transition takes place, the LEV forms and starts to travel along the airfoil's upper side. The location of the LEV can be identified by looking at the c_p and c_f diagrams: at this point during the motion, the LEV is located between $s/c = 0.20$ and $s/c = 0.40$. Pressure fluctuations are still noticeable downstream of the LEV, and the vortex shedding at the trailing edge intensifies. Like for the URANS case, the LEV can be seen as the blue clockwise-circulating region in the reduced vorticity contours, while in the c_p contours the LEV is associated with the suction zone at about one third of the chord. At $\Phi = 90°$, the LEV is transported along the airfoil's upper side and the formation of the tertiary vortex (V3) at half-chord under the LEV can be clearly seen.

At $\Phi = 120°$, as shown in Figure 19, V3 is growing in size and is about to intersect the sheet of negative vorticity connecting the LEV with its vorticity source at the leading edge. Observing the c_p distribution, the suction peak representing the LEV is now located at about $s/c = 0.7$, while in the c_f diagram a large region of reversed flow is identifiable downstream of this point. The LEV then continues to move along the airfoil's upper side, and at $\Phi = 135°$ is located just upstream of the trailing edge, where it starts to promote the TEV roll-up.

At $\Phi = 150°$, the LEV is above the trailing edge, the TEV is completely

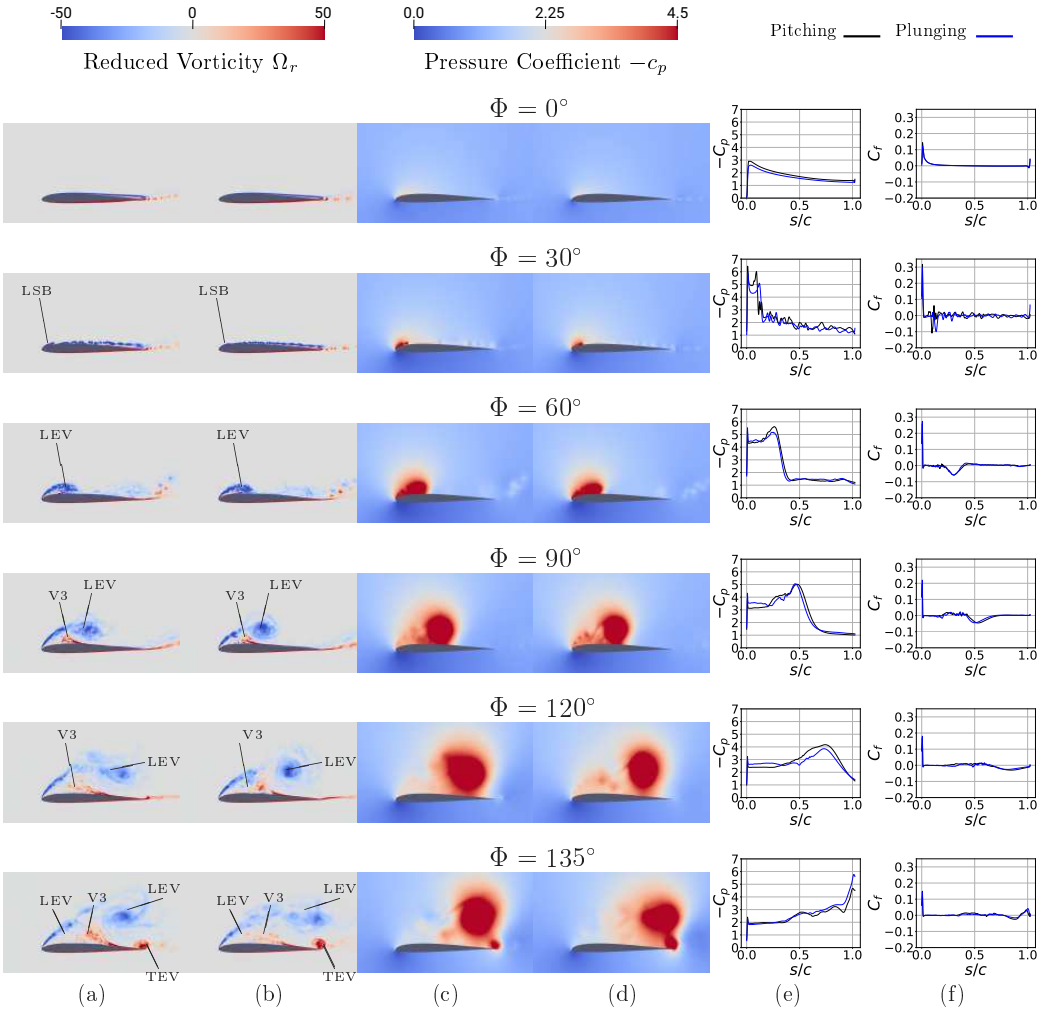

Figure 19: Comparison between phase-averaged pitching and plunging motions for LES calculations, phase-angle from 0 to 135 degrees. Every row is representative of a phase-angle. Columns (a) and (b) report the contour-plots of reduced vorticity for pitching and plunging motions respectively. Columns (c) and (d) show the contour-plots of the pressure coefficient c_p for pitching and plunging motions respectively. Columns (e) and (f) report, for the airfoil's upper side, pressure and skin-friction coefficient distributions as a function of the non-dimensional axial coordinate.

formed and both vortices start to leave the airfoil, while V3 completes its travel over the suction side. With respect to the URANS predictions, the dissipation of this vortical structures is slower in LES simulations, with the effect of larger force and moment coefficients. All three vortices can be seen leaving the airfoil at about $\Phi = 180°$. After $\Phi = 180°$, the c_p and c_f distributions start to flatten out, while a negative vorticity sheet is being released by the leading edge. With respect to URANS predictions, secondary structures (such as the secondary LEV) appear to be dissipated rapidly, and are not easily identifiable in the c_p and c_f plots. Finally, between $\Phi = 210°$ and $\Phi = 270°$, as shown in Figure 20, the boundary layer on the suction side undergoes the reattachment process. After $\Phi = 300°$, the flow over the airfoil recovers its initial state characterized by trailing edge vortex shedding.

4.3. Comparison of URANS and LES results

Results presented in the previous section demonstrated the equivalence of pitching and plunging for an SD7003 airfoil at low Mach number, for a Reynolds number of $6 \cdot 10^4$, and at a reduced frequency of 0.25. The differences between pitching and plunging were found to be minimal, both from URANS (Section 4.1) and LES simulations (Section 4.2), and mainly due to the effect of dynamic cambering in pitching, which causes a wider hysteresis in the pre-static-stall part of the curve, and a marginally larger peak in lift. The phenomenon of dynamic cambering is due to the fact that the flow running on the suction surface experiences a larger cambering due to the fast rotation of the airfoil, thus producing a larger lift. This is possible only when the boundary layer is attached, which is approximately from 240° to somewhere between 0° and 30°, as reported in Figures 15,16, 19, and 20. In this range of phase angles, the cambering-corrected prediction improves for lift and (less) drag coefficients, because the dynamic cambering effect is an inviscid phenomenon, driven by pressure distributions. Outside this range of phase angles, the flow is separated and hence dominated by vortical structures, which prohibit the increase in boundary layer curvature.

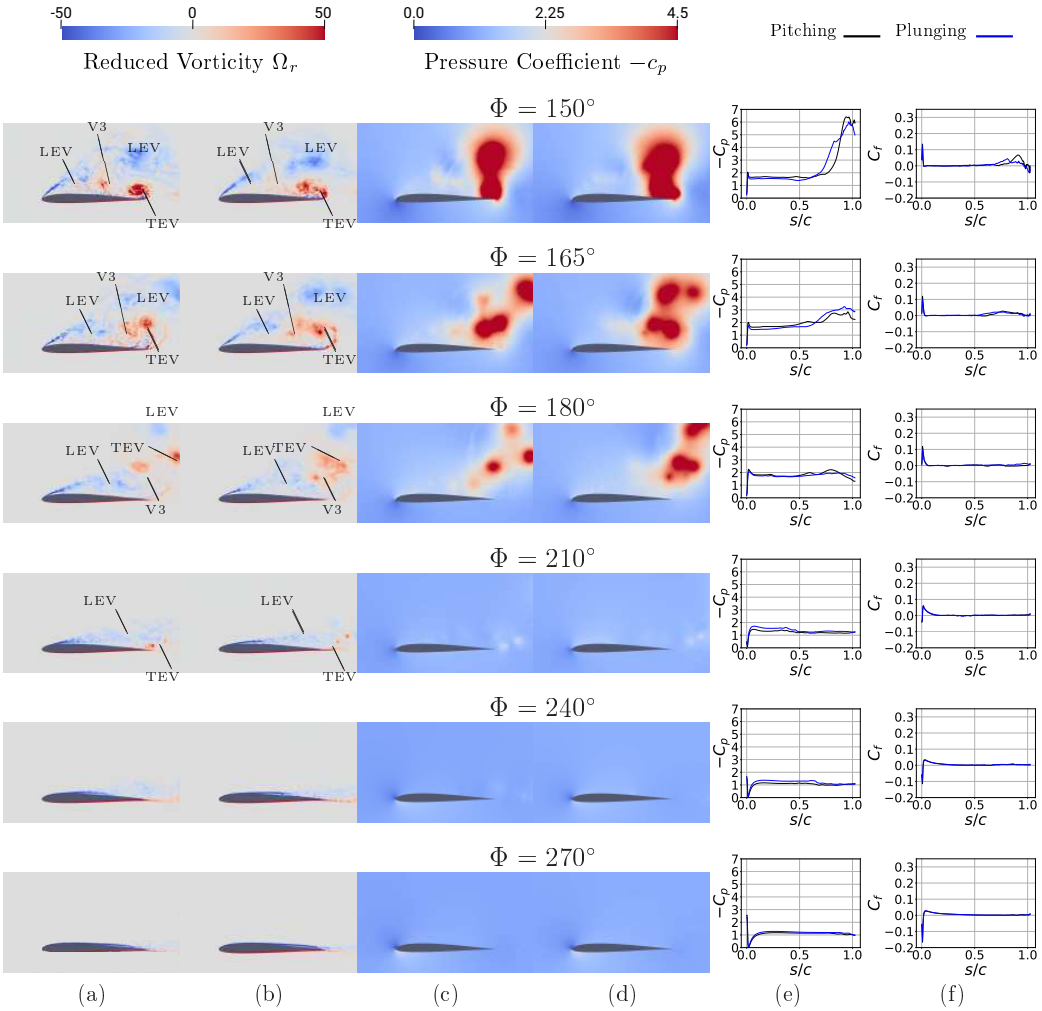

Figure 20: Comparison between phase-averaged pitching and plunging motions for LES calculations, phase-angle from 150 to 270 degrees. Every row is representative of a phase-angle. Columns (a) and (b) report the contour-plots of reduced vorticity for pitching and plunging motions respectively. Columns (c) and (d) show the contour-plots of the pressure coefficient c_p for pitching and plunging motions respectively. Columns (e) and (f) report, for the airfoil's upper side, pressure and skin-friction coefficient distributions as a function of the non-dimensional axial coordinate.

While lift if strongly affected by the behavior of the flow in the first portion of the airfoil, where the larger negative pressures are located, the moment coefficient is more strongly affected by pressures near the trailing edge, where the boundary layer is larger and hence the flow is less responsive to dynamic cambering effects.

More differences can be found when directly comparing the predictions obtained from URANS and LES. Figure 21 presents a comparison of the aerodynamic coefficients in the case of periodic plunging; variability (indicated by means of vertical bars) is significantly larger in the LES curves, due to the direct simulation of smaller vortical structures, which are intrinsically random. The dashed curve represents the results from Visbal's LES analysis [60] which is in good agreement with the present LES solution (red curve). URANS results (blue curve) present differences for values of Φ between 120° and 180°. In particular, the $c_l - \alpha$ predicted by URANS shows two peaks, one negative and one positive, at about 150° and 180° of phase angle, while the values of drag and moment coefficient appear under-predicted, in absolute values. In terms of main flow structures, the differences between URANS and LES start to arise at $\Phi = 90°$, when the first LEV is starting to stretch over the suction side. URANS predict this structure to extend from the leading edge to about half chord, almost attached to the airfoil's surface, with the exception of a thin counter-rotating zone that is starting to gain space under the feeding channel (V3, in its early stages). LES predicts a smaller LEV, located further away from the surface. Instead, the underlying counter-rotating tertiary (V3) is larger and in a more advanced stage of its evolution: a similar state will be reached by the URANS-predicted V3 only at about $\Phi = 120°$. This is evident when comparing the shape of LES and URANS pressure coefficient curves at the two phases (Figures 16 and 20).

Despite being separated earlier from its source, the primary LEV predicted by LES dissipates more gradually than the one predicted by URANS. This leads to LES predicting a much stronger TEV at $\Phi = 150°$, which is

responsible for a larger suction peak at the trailing edge. At the same time, while URANS simulations predict the presence of a strong secondary LEV and a distinct V3, the same structure in LES starts to merge and cancels out, with the effect that only the pressure coefficient distribution predicted by URANS presents an additional suction peak (corresponding to the secondary LEV) at $s/c = 0.4$, followed by a higher c_p region at $s/c = 0.6$. The convection of these separate structures over the suction side of the airfoil is responsible for the negative and positive peaks in c_l distribution, which are not present in LES. At the same time, the larger primary LEV in LES is responsible for a larger negative moment, while the secondary LEV has a smaller influence due to its lower distance from the quarter chord. The secondary LEV in URANS simulations causes a negative friction on the suction surface, which is responsible for an early decrease in drag. At about 150°, the drag coefficient predicted by URANS is about 0.21 (59%) lower than the one predicted by LES, and the negative moment coefficient is about 0.43 (86%) lower.

Between $\Phi = 180°$ and $\Phi = 210°$, the secondary LEV in the URANS simulations still remains very close to the suction side of the airfoil, inducing a low-pressure region that contributes to lift production. At $\Phi = 210°$, the stronger secondary LEV predicted by URANS is also able to induce a new TEV, with consequent additional lift production and a small negative moment spike. The same does not happen in the LES-predicted flow field, where the secondary LEV structure is much less energized. The subsequent motion phases see the boundary layer reattachment over the airfoil's suction side. In this phase, differences between LES and URANS appear less noticeable, both observing the flow fields and the pressure coefficient curves.

While the formation of large scale vortical structure is well predicted by URANS, the evolution and interaction of small structures, which are responsible for the mixing and therefore for the evolution of the large vortices, is less faithful, with the effect of larger fluctuations in lift coefficient, as well as a too

rapid drop in drag and moment coefficients during the phases with decreasing effective angle of attack. The inability of URANS to predict turbulent mixing in largely separated flows in not surprising, as turbulence models were mainly developed for well-attached 2-dimensional flows. Particularly important are the differences in the moment coefficient, as its evolution as a function of the effective angle of attack is crucial to determine the presence of self-induced oscillations, i.e. flutter. McCroskey [83] defines the damping coefficient as follows:

$$\zeta = -\oint c_m \frac{d\alpha}{4\alpha_0^2} \tag{10}$$

The sign of the damping coefficient ζ depends on whether the moment coefficient loop is covered in a counterclockwise or clockwise direction during the motion: the first determines a positive (flutter-inhibiting) contribution, the latter a negative (flutter-inducing) one. If the moment curve forms multiple closed loops as it self-intersects, then each closed loop contributes with its own area and sign to the integral of Eqn. 10. Both URANS and LES predict a negative value of the damping coefficient, as the moment coefficient produces a counterclockwise hysteretic loop in both cases (see Figure 21), but the value predicted by the lower fidelity method is almost half the value predicted by LES (-0.010 versus -0.019).

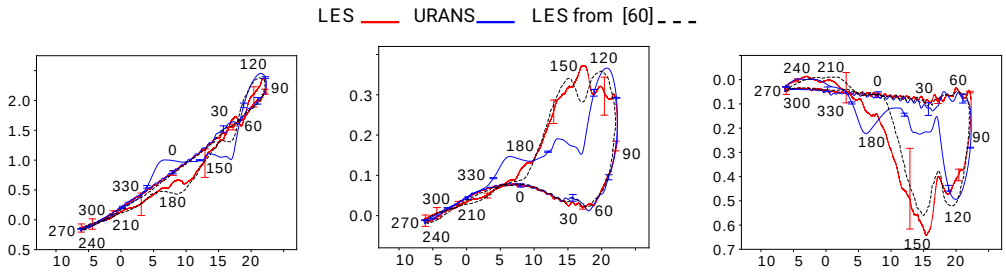

Figure 21: Phase-averaged lift, drag and moment coefficients as a function of the effective angle of attack, for plunging motion; LES vs URANS

Figure 22 presents a comparison of the lift coefficient in the case of peri-

odic plunging, with the experimental measurements reported in [47]. During the phases with decreasing effective angles, the LES results for the lift coefficient match the experimental data significantly better the URANS, where the presence of stronger secondary LEV and V3 causes larger fluctuations in lift coefficient, that are not present in LES simulations and in the experiments. During the phase with increasing effective angles, the experimental data present a larger value for the lift coefficient than both URANS and LES. This larger value (more similar to the value predicted by pitching simulations) was not capture in previous URANS [47] or LES [60] simulations, and might be attributable to geometrical differences between the experimental setup and the numerical simulation.

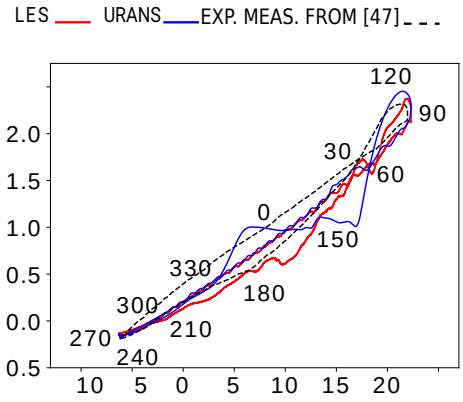

Figure 22: Phase-averaged lift as a function of the effective angle of attack, for plunging motion; LES vs URANS vs experimental measurements from [47]

When defining the laws of motion for equivalent pitching and plunging, the dynamic cambering term in Eq.5 was neglected, based on the discussions in [74]. Nevertheless, some dynamic cambering effects appear to be present at the operating conditions used in this work, as shown in Figures 12 and 17. To verify this hypothesis, the angle of attack for the pitching motion has been corrected following Eq.5, and the result is shown in Figures 23 and 24, for URANS and LES simulations, respectively. From these results, it

appears that some dynamic cambering effect exists only during the pitch-up phase, where the corrected pitching curve provides a better matching to the plunging curve, with respect to the uncorrected one. On the contrary, during the pitch-down phase, the uncorrected pitching curve is already very close to the plunging curve, and adding the correction does not improve the agreement.

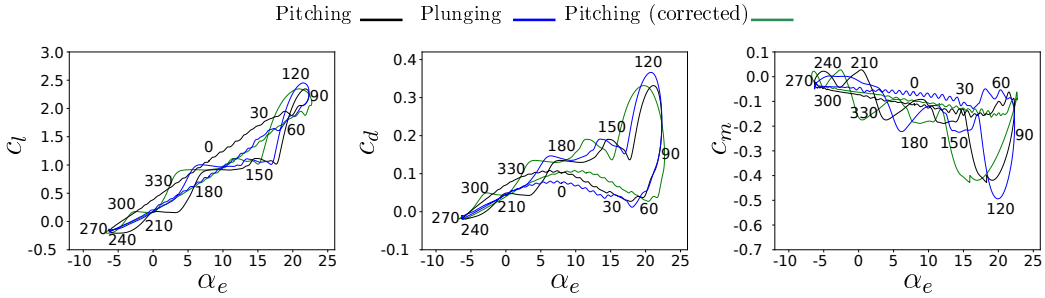

(a) Lift coefficient (b) Drag coefficient (c) Moment coefficient

Figure 23: Phase-averaged lift, drag and moment coefficients as a function of the effective angle of attack, for pitching and plunging motions. Pitching results are presented with and without the dynamic cambering correction; URANS calculations.

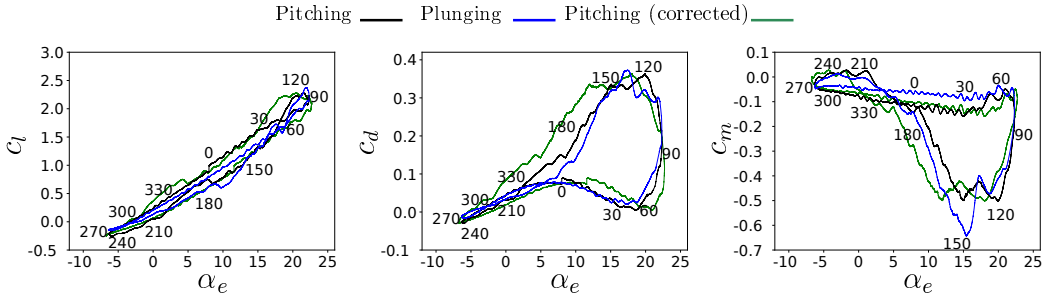

(a) Lift coefficient (b) Drag coefficient (c) Moment coefficient

Figure 24: Phase-averaged lift, drag and moment coefficients as a function of the effective angle of attack, for pitching and plunging motions. Pitching results are presented with and without the dynamic cambering correction; LES calculations.

Figure 25 presents the Q-criterion isosurfaces resulting from the present LES, in the plunging case, colored by means of reduced vorticity. At the beginning of the upstroke ($\Phi = 30°$) the LSB forms near the leading edge,

as visible also from the pressure coefficient curve in Figure 17. Over the whole suction side, Kelvin-Helmholtz instabilities are observable. The LEV can be seen originating from the LSB bursting, fed by vorticity generated at the leading edge at $\Phi = 60°$, and later increasing in size and moving downstream. At $\Phi = 90°$, the V3 vortex is clearly visible as the red region beneath the LEV and slightly upstream of it. It can be seen that, from $\Phi = 60°$ up until $\Phi = 120°$, the primary LEV is the predominant flow structure. Between $\Phi = 120°$ and $\Phi = 150°$, V3 cuts the LEV's feeding channel, accelerating its convection along the suction side, and significantly decreasing the effect it has over the aerodynamic coefficients. At $\Phi = 150°$, V3 can be seen stretching around the front side of the LEV, dividing the dynamic stall flow field in two parts above the suction side. While this happens, the primary LEV is transiting above the trailing edge of the airfoil, inducing the TEV roll-up. From $\Phi = 135°$ to $\Phi = 165°$, the TEV is the most predominant dynamic stall flow feature, as it induces a strong suction peak near the trailing edge. The secondary LEV can also be seen evolving above the airfoil's suction side for $150° < \Phi < 210°$. However, at this point during the motion, the vorticity source at the leading edge is substantially weaker than before, resulting in lower suction. Gradually, the boundary layer reattaches to the suction side, and becomes laminar over larger portions of the airfoil (about 50% at $\Phi = 240°$ and about 80% at $\Phi = 270°$).

4.4. Effect of the Reduced Frequency

The reduced frequency is the most important parameter affecting the behavior of a lifting surface under dynamic stall conditions [83]. In order to investigate the effects of this important parameter, two additional simulations have been performed, for an airfoil undergoing periodic plunging with the same range of angles of attack as in Sections 4.1 and 4.2, but at a reduced frequency 2 and 4 times larger (0.5 and 1.0, respectively), using both 2D URANS and LES approaches. Figures 26 and 27 present a comparison of the mean aerodynamic coefficients predicted with the two approaches, for

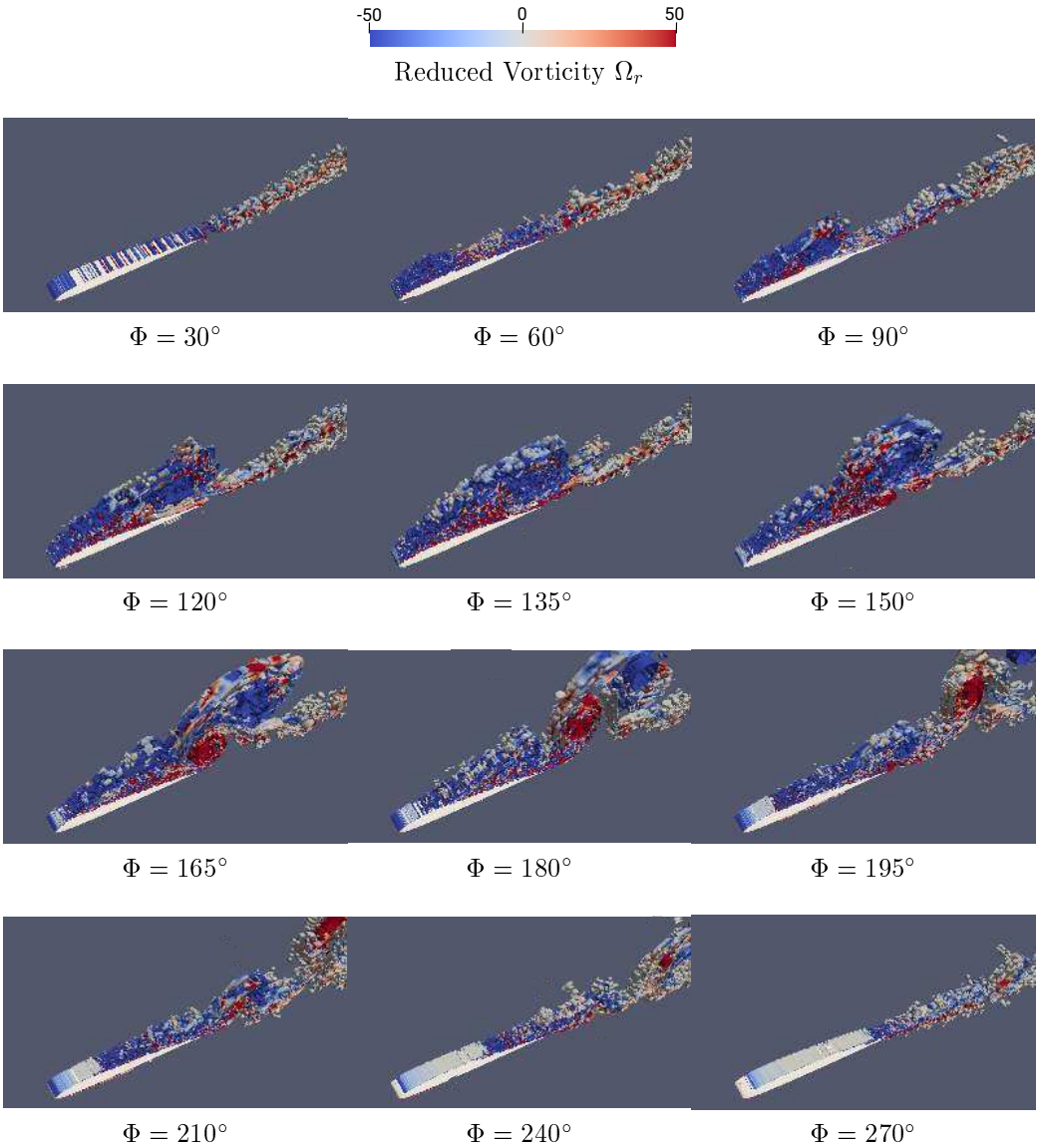

Figure 25: Computed instantaneous three-dimensional flow structure at selected phases of the plunging cycle displayed in terms of a Q-criterion isosurface ($Q = 500$)

the two values of reduced frequency.

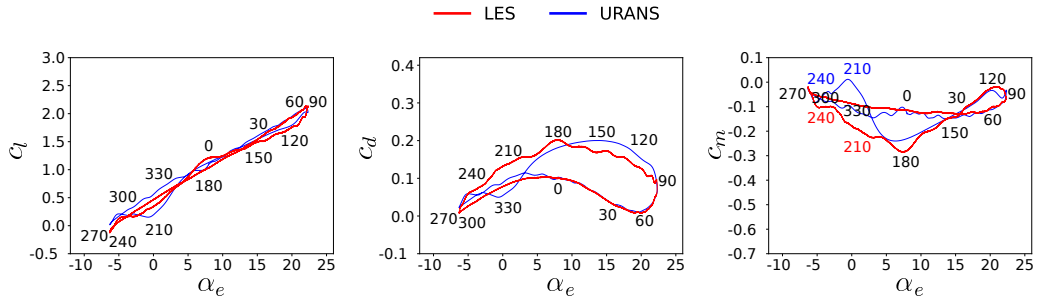

(a) Lift coefficient (b) Drag coefficient (c) Moment coefficient

Figure 26: Phase-averaged lift, drag and moment coefficients as a function of the effective angle of attack, for plunging motion; LES vs URANS for $k = 0.5$

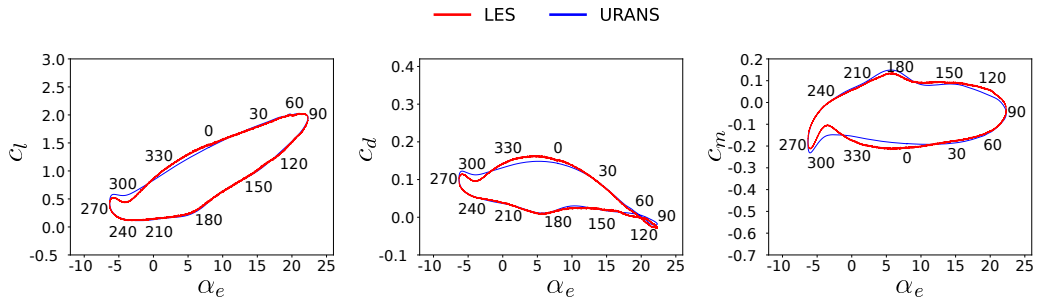

(a) Lift coefficient (b) Drag coefficient (c) Moment coefficient

Figure 27: Phase-averaged lift, drag and moment coefficients as a function of the effective angle of attack, for plunging motion; LES vs URANS for $k = 1.0$

The lift coefficient for the plunging case at $k = 0.5$ (Figure 26) presents only a slight hysteresis in both URANS and LES predictions, and the maximum lift coefficient is slightly lower than the one attained for the reference plunging case at $k = 0.25$. In terms of drag and moment coefficients, the curves pertaining to the case at $k = 0.5$ differ significantly from the ones at $k = 0.25$. The peaks of drag and moment coefficients for values of Φ between 120° and 150° at $k = 0.25$ are not present in the double-frequency curves. In the reference case, this phase interval sees the evolution of the

TEV (Figures 15, 16, 19 and 20), which causes a large increase in drag and pitch-down moment. For the case at $k = 0.5$, there is a significant phase shift in the evolution of the main flow structures, with the LEV reaching the trailing-edge of the airfoil only at $\Phi = 210°$, as shown in Figure 28 ($\Phi = 135°$ for $k = 0.25$). The LEV appears significantly weaker than the one highlighted for the reference case, thus producing a lower peak in the moment coefficient at about $\Phi = 180°$. In terms of comparison between the two CFD techniques, both LEV and TEV in the LES case are stronger than the ones predicted by 2D URANS. In fact, the lower-fidelity simulation predicts a LEV that starts to lose coherence and to dissipate at about $\Phi = 150°$. This causes a large discrepancy in the moment coefficient curves, which affects the overall prediction of the damping behavior. The LES solution predicts a large clockwise loop whose negative contribution is only minimally counteracted by the second, smaller counterclockwise loop. This translates into a net negative damping coefficient ($\zeta = -0.0058$), with the effect that this motion will eventually degenerate into stall flutter according to the LES prediction. On the contrary, the URANS solution predicts 2 counterclockwise loops and a smaller clockwise loop, with a negligible net damping coefficient ($\zeta = 2. \times 10^{-5}$), and hence low risk of flutter associated to this flow condition.

In the plunging case at $k = 1$ (Figure 27), there is an even larger lag between the airfoil movement and the evolution of the flow structures. This can be seen in Figure 29, where the flowfield at all phases is completely dominated by the presence of the LEV. This vortex is weaker with respect to the lower-frequency cases. It departs from the leading-edge at $\Phi = 135°$ and reaches the trailing-edge at a phase of about 300°, inducing a small TEV roll-up. It is interesting to note that, during the LEV's movement along the airfoil's suction side, a relatively high-pressure region is established between the vortex and the trailing edge, which contributes positively to the moment coefficient between $\Phi = 150°$ and $\Phi = 240°$. At $\Phi = 180°$, the LEV is crossing the quarter-chord position. From this position on, the

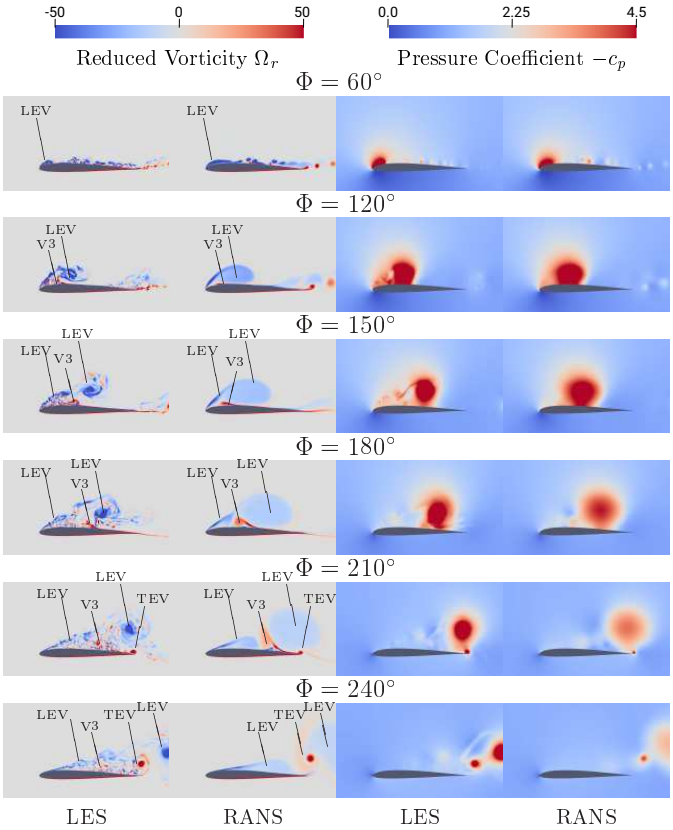

Figure 28: Comparison between vorticity and pressure coefficient predicted by LES and RANS for a plunging motion at $k = 0.5$ at selected values of the phase angle

primary vortex provides a negative moment contribution until it leaves the airfoil. The brief formation of the TEV and the shedding of the LEV are respectively associated with the brief negative moment peak at $\Phi = 300°$ and the subsequent positive spike at $\Phi = 315°$. This out-of-phase interaction between the airfoil and the flow generates a wide hysteresis of the coefficients, which is predicted in a similar way by 2D URANS and LES. The moment coefficient curves predicted by the two techniques for this last case are fairly similar as shown in Figure 27. This high-frequency motion appears to be associated with strong positive damping, as the entire moment coefficient loop is covered in the counterclockwise direction.

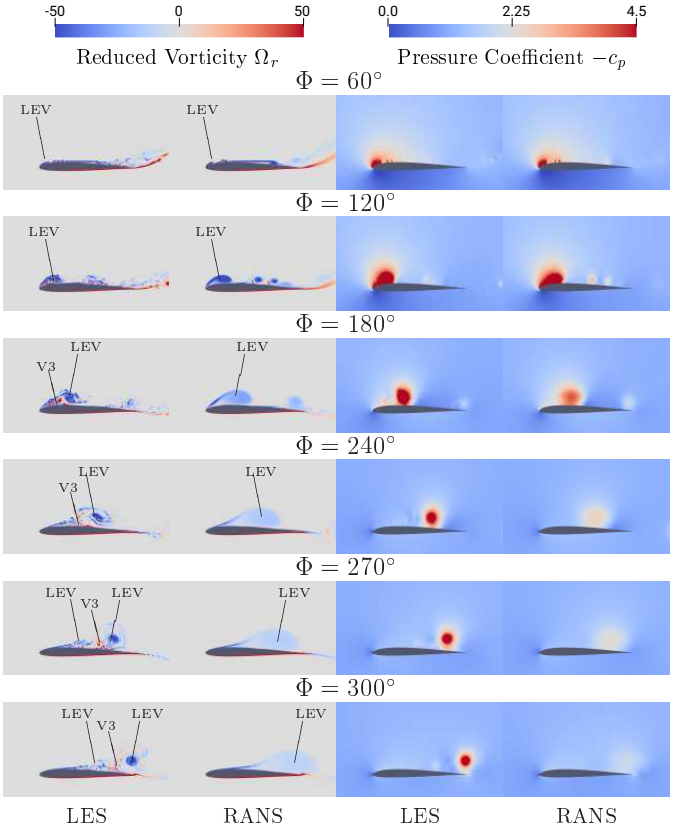

Figure 29: Comparison between vorticity and pressure coefficient predicted by LES and RANS for a plunging motion at $k = 1$ at selected values of the phase angle

Table 3 presents a summary of the comparison between 2D URANS and LES in terms of mean values for the aerodynamic coefficients and damping coefficient. Table 4 summarizes the errors on the mean value of the aerodynamic coefficients, the maximum instantaneous error for the aerodynamic coefficients, and the error for the damping coefficient. The errors are relatively small for the average coefficients' values (the largest being consistently the one for the moment coefficient) and tend to decrease at larger non-dimensional frequencies. The instantaneous errors are significantly larger, but also reduce for larger non-dimensional frequencies. The errors on the damping coefficient are significant for the two lower values of reduced frequency, and almost negligible for the largest value of k.

	2D URANS				LES			
	$\overline{c}_l$	$\overline{c}_d$	$\overline{c}_m$	ζ	$\overline{c}_l$	$\overline{c}_d$	$\overline{c}_m$	ζ
$k = 0.25$	0.913	0.098	0.118	-0.010	0.867	0.101	0.133	-0.019
$k = 0.50$	1.061	0.089	0.098	0.00002	1.017	0.086	0.107	-0.00575
$k = 1.00$	1.037	0.056	0.067	0.02611	1.029	0.055	0.063	0.02655

Table 3: Comparison of 2D URANS and LES predictions of plunging motions at different reduced frequencies

	$\frac{\overline{c}_{l,U}-\overline{c}_{l,L}}{\overline{c}_{l,L}}$	$\frac{\overline{c}_{d,U}-\overline{c}_{d,L}}{\overline{c}_{d,L}}$	$\frac{\overline{c}_{m,U}-\overline{c}_{m,L}}{\overline{c}_{m,L}}$	$\frac{\max(c_{l,U}-c_{l,L})}{\overline{c}_{l,L}}$	$\frac{\max(c_{d,U}-c_{d,L})}{\overline{c}_{d,L}}$	$\frac{\max(c_{m,U}-c_{m,L})}{\overline{c}_{m,L}}$	$\frac{\zeta_U-\zeta_L}{\zeta_L}$
$k = 0.25$	5.31%	-2.99%	-11.20%	74.83%	214.27%	322.18%	-47.64%
$k = 0.50$	4.35%	3.27%	-8.40%	17.24%	88.29%	167.32%	-100.38%
$k = 1.00$	0.77%	3.52%	6.90%	12.82%	30.89%	77.09%	-1.66%

Table 4: Summary of 2D URANS deviations with respect to LES results

5. Conclusion

This work presents a numerical analysis and a comparison of the phenomenon of dynamic stall caused by rapid plunging and pitching motions over an SD7003 airfoil at a Reynolds number of $6 \cdot 10^4$, Mach number of 0.025 and reduced frequency of 0.25, along with a critical description of differences in the prediction of such flow cases between two-dimensional URANS simulations and LES simulations. The remaining parameters defining pitching and plunging motions were selected to produce the same evolution of the

effective angle of attack, between the limits of 5.7° and 22.3°. In dynamic simulations, the equivalence of plunging and pitching motions is sufficiently verified. The evolutions of the force (lift and drag) and moment coefficients present significant similarities, both when computed with URANS and using LES simulations. Also the differences are similar with the two approaches, and correspond to the presence of a dynamic cambering effect for the pitching motion, limited to the pitch-up phase, which causes a larger hysteresis in the lift coefficient, and a more rapid transport of the structures, caused by a stronger tertiary vortex. Focusing on the differences between URANS and LES predictions, it has been concluded that the lower fidelity approach is able to predict the main structures (primary and secondary LEVs, tertiary vortex and TEV), but fails to predict the correct evolution of the tertiary vortex (V3). Moreover, the primary LEV dissipates too rapidly in URANS, after it detaches from its feeding source, which is also the reason behind a weaker TEV. On the contrary, the secondary LEV predicted by URANS appears to be excessively energized. These factors contribute to some noticeable differences between the aerodynamic loads predicted by the two approaches, especially in the vicinity of a phase angle of 150°, near the maximum effective angle of attack.

The effect of an increased non-dimensional frequency on the ability of 2D URANS to predict the aerodynamic characteristics of an airfoil plunging in a periodic motion has been also studied, with two additional simulations at $k = 0.5$ and $k = 1$. It has been found that the differences between 2D URANS and LES reduce for larger non-dimensional frequencies, due to the lower importance of secondary vortical structures, as the behavior tends to be largely dominated by the evolution of the LEV. For the lowest values of k analyzed (0.25 and 0.5), the error in the damping coefficient is large, and this determines the inapplicability of the lower fidelity method for stability analyses.

References

[1] G. Wen, A. Gross, Numerical investigation of deep dynamic stall for a helicopter blade section, AIAA Journal 57 (4) (2019) 1434–1451. doi:10.2514/1.J057686.

[2] C. Singh, D. J. Peake, A. Kokkalis, V. Khodagolian, F. N. Coton, R. A. M. Galbraith, Control of rotorcraft retreating blade stall using air-jet vortex generators, Journal of Aircraft 43 (4) (2006) 1169–1176. doi:10.2514/1.18333.

[3] W. J. McCroskey, The phenomenon of dynamic stall, Tech. Rep. NASA Technical Memorandum 81264, NASA Ames Research Center, Moffett Field, CA, United States (1981).

[4] F. O. Carta, An analysis of the stall flutter instability of helicopter rotor blades, Journal of American Helicopter Society 12 (4) (1967) 1–18.

[5] M. Gaunaa, Unsteady aerodynamic forces on NACA 0015 airfoil in harmonic translatory motion, Ph.D. thesis, Technical University of Denmark. Department of Mechanical Engineering, Fluid Mechanics (2002).

[6] J. Boutet, G. Dimitriadis, X. Amandolese, A modified Leishman–Beddoes model for airfoil sections undergoing dynamic stall at low Reynolds numbers, Journal of Fluids and Structures 93 (2020) 102852. doi:10.1016/j.jfluidstructs.2019.102852.

[7] X. Liu, S. Liang, G. Li, A. Godbole, C. Lu, An improved dynamic stall model and its effect on wind turbine fatigue load prediction, Renewable Energy 156 (2020) 117 – 130. doi:10.1016/j.renene.2020.04.040.

[8] J. Ekaterinaris, N. Sorensen, F. Rasmussen, Numerical investigation of airfoil dynamic stall in simultaneous harmonic oscillatory and translatory motion, Journal of Solar Energy Engineering, Transactions of the ASME 120 (1) (1998) 75–83. doi:10.1115/1.2888050.

[9] H. Akhlaghi, M.-R. Soltani, M.-J. Maghrebi, Transitional boundary layer study over an airfoil in combined pitch-plunge motions, Aerospace Science and Technology 98 (2020) 105694. doi:10.1016/j.ast.2020.105694.

[10] J. T. Petersen, , H. A. Madsen, A. Bkjorck, P. Enevoldsen, S. Ove, H. Ganader, D. Winkelaar, Prediction of dynamic loads and induced vibrations in stall, Tech. Rep. Riso Rport R-1045, Riso National Laboratory, Roskilde, Denmark (1998).

[11] R. Zahn, M. Winter, M. Zieher, C. Breitsamter, Application of a long short-term memory neural network for modeling transonic buffet aerodynamics, Aerospace Science and Technology 113 (2021) 106652. doi:10.1016/j.ast.2021.106652.

[12] C. Zhu, J. Chen, J. Wu, T. Wang, Dynamic stall control of the wind turbine airfoil via single-row and double-row passive vortex generators, Energy 189 (2019) 116272. doi:10.1016/j.energy.2019.116272.

[13] J. Zhong, J. Li, P. Guo, Y. Wang, Dynamic stall control on a vertical axis wind turbine aerofoil using leading-edge rod, Energy 174 (2019) 246 – 260. doi:10.1016/j.energy.2019.02.176.

[14] L. Wang, S. Fu, Detached-eddy simulation of flow past a pitching NACA 0015 airfoil with pulsed actuation, Aerospace Science and Technology 69 (2017) 123 – 135. doi:10.1016/j.ast.2017.06.002.

[15] L. Guoqiang, Y. Shihe, Large eddy simulation of dynamic stall flow control for wind turbine airfoil using plasma actuator, Energy 212 (2020) 118753. doi:10.1016/j.energy.2020.118753.

[16] M. De Giorgi, V. Motta, A. Suma, Influence of actuation parameters of multi-dbd plasma actuators on the static and dynamic behaviour of

an airfoil in unsteady flow, Aerospace Science and Technology 96 (2020) 105587. doi:10.1016/j.ast.2019.105587.

[17] J. Ekaterinaris, Prediction of active flow control performance on airfoils and wings, Aerospace Science and Technology 8 (5) (2004) 401–410. doi:10.1016/j.ast.2004.02.003.

[18] Y. Li, N. Qin, Airfoil gust load alleviation by circulation control, Aerospace Science and Technology 98 (2020) 105622. doi:10.1016/j.ast.2019.105622.

[19] S. Cao, N. Dang, Z. Ren, J. Zhang, Y. Deguchi, Lagrangian analysis on routes to lift enhancement of airfoil by synthetic jet and their relationships with jet parameters, Aerospace Science and Technology 104 (2020) 105947. doi:10.1016/j.ast.2020.105947.

[20] D. Asadi, T. Farsadi, Active flutter control of thin walled wing-engine system using piezoelectric actuators, Aerospace Science and Technology 102 (2020) 105853. doi:10.1016/j.ast.2020.105853.

[21] W. Kang, M. Xu, W. Yao, J. Zhang, Lock-in mechanism of flow over a low-Reynolds-number airfoil with morphing surface, Aerospace Science and Technology 97 (2020) 105647. doi:10.1016/j.ast.2019.105647.

[22] J. Lei, J. Zhang, J. Niu, Effect of active oscillation of local surface on the performance of low Reynolds number airfoil, Aerospace Science and Technology 99 (2020) 105774. doi:10.1016/j.ast.2020.105774.

[23] Y. Ouyang, Y. Gu, X. Kou, Z. Yang, Active flutter suppression of wing with morphing flap, Aerospace Science and Technology 110 (2021) 106457. doi:10.1016/j.ast.2020.106457.

[24] V. Raul, L. Leifsson, Surrogate-based aerodynamic shape optimization for delaying airfoil dynamic stall using Kriging regression and

infill criteria, Aerospace Science and Technology 111 (2021) 106555. doi:10.1016/j.ast.2021.106555.

[25] F. Fusi, P. M. Congedo, A. Guardone, G. Quaranta, Assessment of robust optimization for design of rotorcraft airfoils in forward flight, Aerospace Science and Technology 107 (2020) 106355. doi:10.1016/j.ast.2020.106355.

[26] C. Kang, Y. Baik, L. Bernal, M. V. Ol, W. Shyy, Fluid dynamics of pitching and plunging airfoils of Reynolds number between 1×10^4 and 6×10^4, in: 47th AIAA Aerospace Sciences Meeting including The New Horizons Forum and Aerospace Exposition, Orlando, Florida, USA, 2009. doi:10.2514/6.2009-536.

[27] J. M. Anderson, K. Streitlien, D. S. Barrett, M. S. Triantafyllou, Oscillating foils of high propulsive efficiency, Journal of Fluid Mechanics 360 (1998) 41–72. doi:10.1017/S0022112097008392.

[28] M. J. Lighthill, On the Weis-Fogh mechanism of lift generation, Journal of Fluid Mechanics 60 (1) (1973) 1–17. doi:10.1017/S0022112073000017.

[29] W. Chen, W. Qiao, Z. Wei, Aerodynamic performance and wake development of airfoils with wavy leading edges, Aerospace Science and Technology 106 (2020) 106216. doi:https://doi.org/10.1016/j.ast.2020.106216.

[30] W. Geissler, B. G. van der Wall, Dynamic stall control on flapping wing airfoils, Aerospace Science and Technology 62 (2017) 1 – 10. doi:10.1016/j.ast.2016.12.008.

[31] R. Sankarasubramanian, A. Sridhar, M. Prashanth, A. Mohammad, R. K. Velamati, L. Vaitla, Influence of thickness on performance characteristics of non-sinusoidal plunging motion of symmet-

ric airfoil, Aerospace Science and Technology 81 (2018) 333 – 347. doi:10.1016/j.ast.2018.08.007.

[32] J. Niu, J. Lei, T. Lu, Numerical research on the effect of variable droop leading-edge on oscillating NACA 0012 airfoil dynamic stall, Aerospace Science and Technology 72 (2018) 476–485. doi:10.1016/j.ast.2017.11.030.

[33] T. Zhou, E. Dowell, S. shan Feng, Computational investigation of wind tunnel wall effects on buffeting flow and lock-in for an airfoil at high angle of attack, Aerospace Science and Technology 95 (2019) 105492. doi:10.1016/j.ast.2019.105492.

[34] T. Kinsey, G. Dumas, Parametric study of an oscillating airfoil in a power-extraction regime, AIAA Journal 46 (6) (2008) 1318–1330. doi:10.2514/1.26253.

[35] J. Wu, S. C. Yang, C. Shu, N. Zhao, Y. W. W., Ground effect on the power extraction performance of a flapping wing biomimetic energy generator, Journal of Fluids and Structures 54 (2015) 247–262. doi:10.1016/j.jfluidstructs.2014.10.018.

[36] I. Fenercioglu, O. Cetiner, Categorization of flow structures around a pitching and plunging airfoil, Journal of Fluids and Structures 31 (2012) 92 – 102. doi:10.1016/j.jfluidstructs.2012.03.001.

[37] A. Sharma, M. R. Visbal, Airfoil thickness effects on dynamic stall onset, in: 23rd AIAA Computational Fluid Dynamics Conference, Denver, CO, USA, 2017. doi:10.2514/6.2017-3957.

[38] K. Kaufmann, C. B. Merz, A. D. Gardner, Dynamic stall simulations on a pitching finite wing, Journal of Aircraft 54 (4) (2017) 1303–1316. doi:10.2514/1.C034020.

[39] I. Andreu Angulo, P. J. Ansell, Influence of aspect ratio on dynamic stall of a finite wing, AIAA Journal 57 (7) (2019) 2722–2733. doi:10.2514/1.J057792.

[40] S. I. Benton, M. R. Visbal, Effects of compressibility on dynamic-stall onset using large-eddy simulation, in: AIAA Scitech Forum, San Diego, CA, USA, 2019. doi:10.2514/6.2019-0301.

[41] G. Z. McGowan, K. Granlund, M. V. Ol, A. Gopalarathnam, J. R. Edwards, Investigations of lift-based pitch-plunge equivalence for airfoils at low Reynolds numbers, AIAA Journal 49 (7) (2011) 1511–1524. doi:10.2514/1.J050924.

[42] K. Granlund, M. V. Ol, C. Cox, A. Gopalarathnam, J. R. Edwards, The validity bounds of analytical force and moment predictions for pitch- and plunge oscillating low Reynolds number airfoils, in: AIAA Atmospheric Flight Mechanics Conference, Grapevine, TX, USA, 2017. doi:10.2514/6.2010-8126.

[43] T. Theodorsen, General theory of aerodynamic instability and the mechanism of flutter, Tech. Rep. NACA reoirt 496, National Advisory Committee for Aeronautics (1935).

[44] S. Brunton, C. Rowley, Modeling the unsteady aerodynamic forces on small-scale wings, in: 47th AIAA Aerospace Sciences Meeting including The New Horizons Forum and Aerospace Exposition, Orlando, FL, USA, 2009. doi:10.2514/6.2009-1127.

[45] G. McGowan, A. Gopalarathnam, M. V. Ol, J. R. Edwards, Analytical, computational, and experimental investigations of equivalence between pitch and plunge motions for airfoils at low Reynolds numbers, in: 47th AIAA Aerospace Sciences Meeting including The New Horizons Forum and Aerospace Exposition, Orlando, FL, USA, 2009. doi:10.2514/6.2009-535.

[46] L. Bernal, M. V. Ol, D. Szczublewski, C. Cox, Unsteady force measurements in pitching-plunging airfoils, in: 39th AIAA Fluid Dynamics Conference, San Antonio, TX, USA, 2009. doi:10.2514/6.2009-4031.

[47] M. V. Ol, L. Bernal, C. Kang, S. Wei, Shallow and deep dynamic stall for flapping low Reynolds number airfoils, Experiments in Fluids 46 (5) (2009) 883–901. doi:10.1007/s00348-009-0660-3.

[48] J. Young, J. C. S. Lai, Mechanisms influencing the efficiency of oscillating airfoil propulsion, AIAA Journal 45 (7) (2007) 1695–1702. doi:10.2514/1.27628.

[49] L. W. Carr, K. W. McAlister, W. J. McCroskey, Mechanisms influencing the efficiency of oscillating airfoil propulsion, Tech. Rep. NASA Technical Note D-8382, NASA Ames Research Center, Moffett Field, CA, United States (1977).

[50] M. Acharya, M. H. Metwally, Unsteady pressure field and vorticity production over a pitching airfoil, AIAA Journal 30 (2) (1992) 403–411. doi:10.2514/3.10931.

[51] J. M. Yu, T. S. Leu, J. J. Miau, Investigation of reduced frequency and freestream turbulence effects on dynamic stall of a pitching airfoil, Journal of Visualization 20 (1) 31–44. doi:10.1007/s12650-016-0366-6.

[52] W. Wang, S. Cao, N. Dang, J. Zhang, Y. Deguchi, Study on dynamics of vortices in dynamic stall of a pitching airfoil using Lagrangian coherent structures, Aerospace Science and Technology 113 (2021) 106706. doi:10.1016/j.ast.2021.106706.

[53] C. Tseng, H. Hu, Flow dynamics of a pitching foil by Eulerian and Lagrangian viewpoints, AIAA Journal 54 (2) (2016) 712–727. doi:10.2514/1.J053619.

[54] G. N. Barakos, D. Drikakis, Computational study of unsteady turbulent flows around oscillating and ramping aerofoils, International Journal for Numerical Methods in Fluids 42 (2) (2003) 163–186. doi:10.1002/fld.478.

[55] T. Kim, S. Kim, J. Lim, S. Jee, Numerical investigation of compressibility effect on dynamic stall, Aerospace Science and Technology 105 (2020) 105918. doi:10.1016/j.ast.2020.105918.

[56] M. Chandrasekhara, M. Wilder, L. Carr, Reynolds number influence on 2-d compressible dynamic stall, in: 34th Aerospace Sciences Meeting and Exhibit, Reno, NV, USA, 1996. doi:10.2514/6.1996-73.

[57] C. Marongiu, R. Tognaccini, Simulation of the dynamic stall at low Reynolds number, in: 48th AIAA Aerospace Sciences Meeting Including the New Horizons Forum and Aerospace Exposition, Orlando, FL, USA, 2010. doi:10.2514/6.2010-513.

[58] M. S. Chandrasekhara, S. Ahmed, Velocity and vorticity distributions over an oscillating airfoil under compressible dynamic stall, AIAA Journal 31 (6) (1993) 995–996. doi:10.2514/3.11719.

[59] M. R. Visbal, D. J. Garmann, Analysis of dynamic stall on a pitching airfoil using high-fidelity large-eddy simulations, AIAA Journal 56 (1) (2018) 46–63. doi:10.2514/1.J056108.

[60] M. R. Visbal, Numerical investigation of deep dynamic stall of a plunging airfoil, AIAA Journal 49 (10) (2011) 2152–2170. doi:10.2514/1.J050892.

[61] T. Ghisu, F. Cambuli, P. Puddu, I. Virdis, M. Carta, Discussion: "Unsteady RANS simulations of wells turbine under transient flow conditions", Journal of Offshore Mechanics and Arctic Engineering 141 (4). doi:10.1115/1.4042875.

[62] W. Mallik, D. E. Raveh, Aerodynamic damping investigations of light dynamic stall on a pitching airfoil via modal

analysis, Journal of Fluids and Structures 98 (2020) 103111. doi:10.1016/j.jfluidstructs.2020.103111.

[63] P. Sidlof, V. Vlcek, M. Stepan, Experimental investigation of flow-induced vibration of a pitch–plunge NACA 0015 airfoil under deep dynamic stall, Journal of Fluids and Structures 67 (2016) 48 – 59. doi:10.1016/j.jfluidstructs.2016.08.011.

[64] L. W. Carr, K. W. McAlister, W. J. McCroskey, Analysis of the development of dynamic stall based on oscillating airfoil experiments, NASA Technical Note D-8382 (January) (1977) 1–99, iSBN: 0821302450.

[65] J. Albertson, T. Troutt, C. Kedzie, Unsteady aerodynamic forces at low airfoil pitching rates, in: 6th Applied Aerodynamics Conference, Williamsburg, VA, USA, 1988. doi:10.2514/6.1988-2579.

[66] A. J. Niven, R. A. Galbraith, The effect of pitch rate on the dynamic stall of a modified NACA 23012 aerofoil and comparison with the unmodified case, International Journal of Rotorcraft and Powered Lift Aircraft 11 (4) (1987) 751–759.

[67] J. Leishman, Principles of Helicopter Aerodynamics, Cambridge Aerospace Series, Cambridge University Press, 2002.

[68] D. Rival, C. Tropea, Characteristics of pitching and plunging airfoils under dynamic-stall conditions, Journal of Aircraft 47 (1) (2010) 80–86. doi:10.2514/1.42528.

[69] J. Panda, K. B. M. Q. Zaman, Experimental investigation of the flow field of an oscillating airfoil and estimation of lift from wake surveys, Journal of Fluid Mechanics 265 (1994) 65–95. doi:10.1017/S0022112094000765.

[70] D. Kamari, M. Tadjfar, A. Madadi, Optimization of SD7003 airfoil performance using TBL and CBL at low Reynolds numbers, Aerospace Science and Technology 79 (2018) 199–211. doi:10.1016/j.ast.2018.05.049.

[71] S. I. Benton, M. R. Visbal, Understanding abrupt leading edge separation as a mechanism for the onset of dynamic stall, in: 2018 AIAA Aerospace Sciences Meeting. doi:10.2514/6.2018-0356.

[72] J. Tyacke, P. Tucker, Future use of large eddy simulation in aero-engines, Journal of Turbomachinery 137 (8). doi:10.1115/1.4029363.

[73] M. Galbraith, M. Visbal, Implicit large eddy simulation of low Reynolds number flow past the sd7003 airfoil, in: 46th AIAA Aerospace Sciences Meeting and Exhibit, Reno, NV, USA, 2008. doi:10.2514/6.2008-225.

[74] D. Rival, C. Tropea, Characteristics of pitching and plunging airfoils under dynamic-stall conditions, in: 47th AIAA Aerospace Sciences Meeting including The New Horizons Forum and Aerospace Exposition, Orlando, FL, USA. doi:10.2514/6.2009-537.

[75] Y. M. Lee, J. H. Lee, L. P. Raj, J. H. Jo, R. S. Myong, Large-eddy simulations of complex aerodynamic flows over multi-element iced airfoils, Aerospace Science and Technology 109 (2021) 106417. doi:https://doi.org/10.1016/j.ast.2020.106417.

[76] Y. Zhang, H. Chen, S. Fu, W. Dong, Numerical study of an airfoil with riblets installed based on large eddy simulation, Aerospace Science and Technology 78 (2018) 661–670. doi:https://doi.org/10.1016/j.ast.2018.05.013.

[77] P. Itsariyapinyo, R. N. Sharma, Large eddy simulation of a naca0015 circulation control airfoil using synthetic jets, Aerospace Science and Technology 82-83 (2018) 545–556. doi:https://doi.org/10.1016/j.ast.2018.09.039.

[78] A. Ebrahimi, M. Hajipour, Flow separation control over an airfoil using dual excitation of dbd plasma actuators, Aerospace Science and Technology 79 (2018) 658–668. doi:https://doi.org/10.1016/j.ast.2018.06.019.

[79] C. du Plessis, S. J. Van der Spuy, H. C. R. Reuter, On the effect of the correction of modelled airfoil tonal noise for a spanwise extension, Aerospace Science and Technology 118 (2021) 107033. doi:https://doi.org/10.1016/j.ast.2021.107033.

[80] A. Inc., Ansys Fluent User Guide.

[81] A. Inc., Ansys Fluent Theory Guide.

[82] M. Ol, B. Mcauliffe, E. Hanff, U. Scholz, C. Kähler, Comparison of laminar separation bubble measurements on a low reynolds number airfoil in three facilities, AIAA paper 5149. doi:10.2514/6.2005-5149.

[83] W. J. McCroskey, The Phenomenon of Dynamic Stall, NASA Technical Memorandum 81264 (1981) 1–28ISBN: 978-0-06-163265-5. doi:10.1080/6008555886.